2024-08-01

Determining Heterogeneous Growth Rates Of Brucite On Magnesia Using Multiharmonic Qcm-D And X-Ray Scattering Methods

Pedro Josue Hernandez Penagos
University of Texas at El Paso

DETERMINING HETEROGENEOUS GROWTH RATES OF BRUCITE ON MAGNESIA USING MULTIHARMONIC QCM-D AND X-RAY SCATTERING METHODS

PEDRO JOSUE HERNANDEZ PENAGOS

Master's Program in Physics

APPROVED:

José Leobardo Bañuelos, Ph.D., Chair

Ahmed El-Gendy, Ph.D.

Benjamin Brunner, Ph.D.

Stephen L. Crites, Jr., Ph.D.
Dean of the Graduate School

Dedication

This thesis is wholeheartedly dedicated to my beloved parents, whose unwavering love and selfless support have been my guiding light through every decision I have made. Their strength has empowered me to surmount every challenge I have encountered, and their faith in me has remained steadfast, even when I faltered.

I also dedicate this work to my friends, who have stood by me through thick and thin. Their support has been constant in both personal and academic challenges. Their encouragement was a key factor in my journey to complete this thesis, and their belief in my potential has been a source of endless inspiration.

DETERMINING HETEROGENEOUS GROWTH RATES OF BRUCITE ON MAGNESIA USING MULTIHARMONIC QCM-D AND X-RAY SCATTERING METHODS

by

PEDRO JOSUE HERNANDEZ PENAGOS, BS.

THESIS

Presented to the Faculty of the Graduate School of

The University of Texas at El Paso

in Partial Fulfillment

of the Requirements

for the Degree of

MASTER OF SCIENCE

Department of Physics

THE UNIVERSITY OF TEXAS AT EL PASO

August 2024

Acknowledgements

I extend my deepest gratitude to my faculty mentor, Dr. José Leobardo Bañuelos, whose guidance was the cornerstone of this research project. His unwavering patience, motivational support, and insightful understanding of my capabilities and areas for growth were instrumental during my tenure at UTEP.

My heartfelt thanks go to Dr. Juliane Weber, Dr. Ilia Ivanov, and Dr. Ke Yuan for their invaluable patience and counsel throughout my Graduate Summer Research Internship at Oak Ridge National Laboratory. I am also immensely grateful to all the scientists and staff at Oak Ridge National Laboratory, whose collaboration was crucial in the fruition of this thesis.

I must equally acknowledge my laboratory colleagues: Daniel, Masiel, Silvestre, Emiliano, and Alan. Their camaraderie made countless hours in the laboratory not only bearable but enjoyable, enriching my research experience beyond measure.

I am also thankful to my professors for their exceptional instruction during my graduate studies. Being your pupil and receiving your wisdom has been a great honor.

Lastly, I express my sincere appreciation to the U.S. Department of Energy, Office of Science, Basic Energy Sciences, Material Science and Engineering Division for their generous funding that supported this research endeavor.

Abstract

The Earth's temperature has increased in the last six decades mainly due to the emissions of greenhouse gases, including carbon dioxide (CO_2). Mineral looping using magnesium oxide (MgO) is a promising approach for direct air capture (DAC) of CO_2 from the atmosphere at the $GtCO_2$/yr scale. The presence of humidity during the carbonation process will lead to a reaction between the MgO and water resulting in magnesium hydroxide formation, $Mg(OH)_2$, growing over the MgO surface forming a shell-like structure. The influence of temperature and relative humidity variation on heterogeneous nucleation and crystal growth kinetics of $Mg(OH)_2$ on MgO is not well understood under environmentally/DAC-relevant conditions. In this thesis, quartz crystal microbalance (QCM) commercial crystals were coated with a ~90nm-thick MgO film using pulsed laser deposition (PLD). Experiments to investigate brucite formation using multiharmonic QCM with Dissipation analysis (QCM-D) were conducted by flowing deionized water at 20 µl/min over the MgO film, as well as under water vapor exposure. Results of QCM-D analysis using first-order kinetic models will be presented. Batch experiments were also conducted using three distinct types of MgO powder. Similar quantities of each powder were exposed to varying levels of relative humidity (RH) over different durations. The mass changes in these samples were meticulously measured. Subsequently, the results were analyzed using first-order kinetic models. These samples were analyzed using small angle x-ray scattering (SAXS) and wide-angle x-ray scattering (WAXS) to relate molecular and nanoscale structural changes to the QCM studies. This work allowed estimates of growth rates by analyzing the time-dependence of mass loss under each experimental condition.

Table of Contents

List of Tables

List of Figures

1. Introduction

As of December of 2023, the concentration of carbon dioxide (CO_2) in the atmosphere has reached 421.86 parts per million by volume (ppm) an increase of 33.5% since 1959 [1]. Current CO_2 emissions levels exceeded 37 $GtCO_2$/year [2]. To decrease this trend and thus help to mitigate climate change, a project for direct air capture (DAC) of this greenhouse gas from the atmosphere has been developed [3], [4], [5].

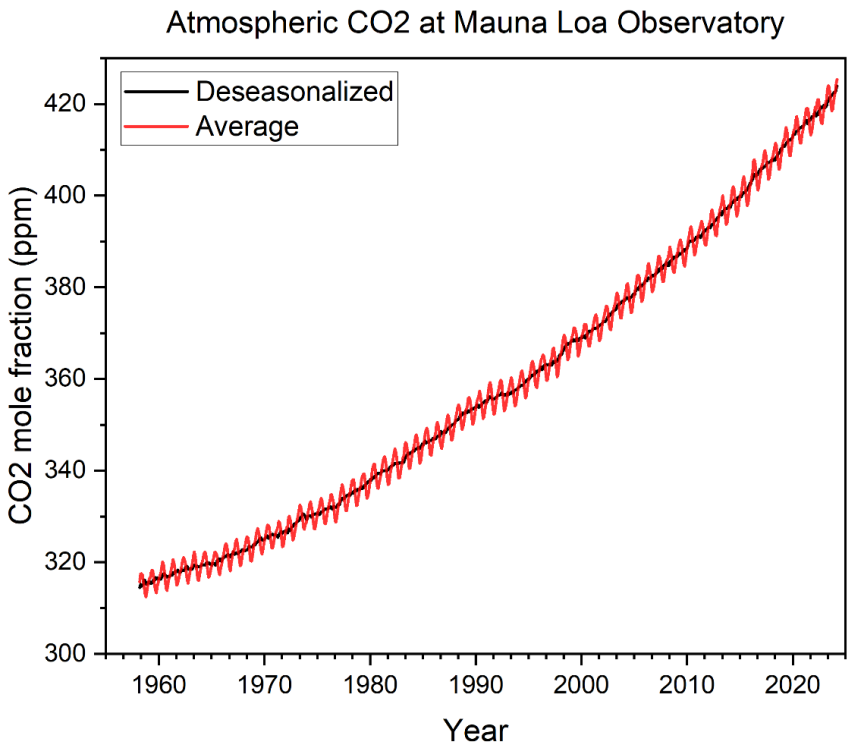

Figure 1: Yearly mean carbon dioxide measured at Mauna Loa Observatory, Hawaii. [1].

Mineral looping is a process that has the potential of removing CO_2 at a rate of $GtCO_2$/year [6] and is briefly described below. An MgO (magnesia) layer is placed in the environment, where it will react with atmospheric CO_2, resulting in the formation of $MgCO_3$ (magnesite). After approximately a year, the magnesite is collected and put into a calciner. Here, the material is heated

at 500 ˚C – 1200 ˚C producing MgO and CO_2 again. The CO_2 is then stored, and the magnesia is placed again in the environment, repeating the process.

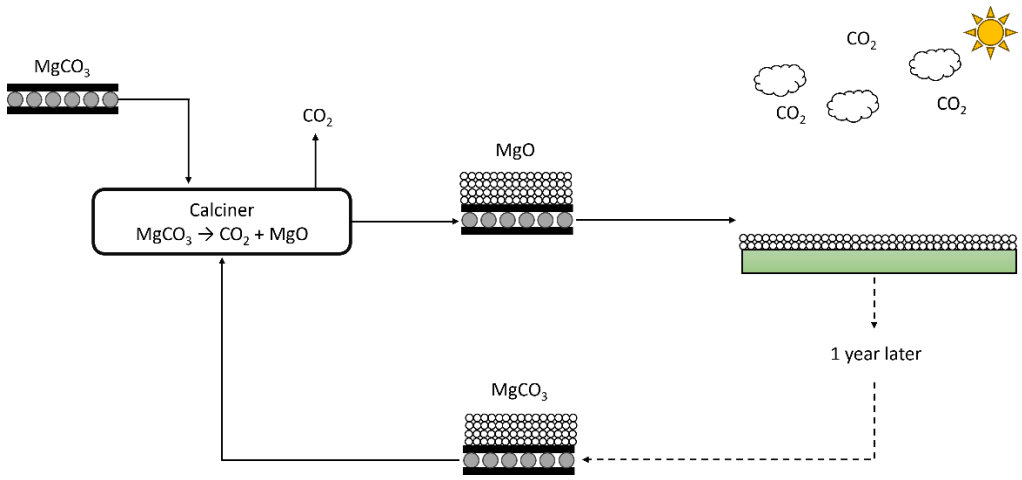

Figure 2: Envisioned MgO looping process. [6].

This mineral looping process has an estimated efficiency of 90-95% of the MgO that will be recollected. This process has an estimated cost of \$46-\$159/tCO_2 and has the potential of removing 2-3 GtCO_2/year. However, MgO reactivity is affected after undergoing several calcination processes with a 5-7% drop in efficiency after 10 cycles [7], [8] or 12-19% after 6 cycles [9], [10]. Some of the reasons magnesia is used in this mineral looping process is that its carbonation process requires less energy input to release the CO_2 from the carbonate in comparison with other minerals as CaO [5].

$$MgO + CO_2 \rightarrow MgCO_3 + 118\ kJ/mole \quad (1)$$

$$CaO + CO_2 \rightarrow CaCO_3 + 179\ kJ/mole \quad (2)$$

$MgCO_3$ calcination temperature (540 ˚C) [11] is lower than that for $CaCO_3$ (825 ˚C) [12]. Also, it has been proven that the amount of magnesium oxide (3.4 t) required to capture produced by

burning one ton of carbon is less than the one required for calcium oxide (4.7 t) [5]. Despite the advantage this process possesses, there are still some fundamental aspects that are not well understood and that affect the overall efficiency of mineral looping. As mentioned before, a magnesia layer is placed in the environment to react with CO_2, but the former can also react with H_2O (water) present in the form of humid air, rainfall, or surface water runoff. The reaction (I) of these two substances results in the formation of $Mg(OH)_2$ (brucite) in a process known as hydroxylation reaction of MgO.

Reaction I $$MgO + H_2O \rightarrow Mg(OH)_2 \quad (3)$$

Currently, it is unknown how the formation of brucite affects the reaction of the substances that take place in the mineral looping process.

Related to this project, but not considered in this thesis, are other two reactions: (II) $Mg(OH)_2$ dissolution and (III) $MgCO_3$ precipitation:

Reaction II $$Mg(OH)_2 + 6H_2O \rightarrow Mg(OH_2)_6{}^{2+} + 2OH^- \quad (4)$$

Reaction III $$Mg(OH_2)_6{}^{2+} + CO_2 + 2OH^- \rightarrow MgCO_3 + 7H_2O \quad (5)$$

Other reactions can occur depending on the amount of water present in the environment. These reactions result in the formation of different magnesium carbonate phases [11].

Nesquehonite $$Mg(OH)_2 + CO_2 + 2H_2O \rightarrow MgCO_3 \cdot 3H_2O \quad (6)$$

Hydromagesite $$5Mg(OH)_2 + 4CO_2 \rightarrow 4MgCO_3 \cdot Mg(OH)_2 \cdot 4H_2O \quad (7)$$

Dypongite $$5Mg(OH)_2 + 4CO_2 + 6H_2O \rightarrow 4MgCO_3 \cdot Mg(OH)_2 \cdot 5H_2O \quad (8)$$

Experiments to investigate brucite formation using multiharmonic QCM with Dissipation analysis (QCM-D) were conducted by flowing deionized water at 20 µl/min over the MgO film, as well as under water vapor exposure. This work allowed estimates of dissolution and growth rates by analyzing the time-dependence of mass loss under each experimental condition. Results of QCM analysis using first and second order kinetic models will be presented.

Small-angle x-ray scattering (SAXS) and wide-angle x-ray scattering (WAXS) were also performed to describe the molecular and nanoscale structural changes to the QCM studies.

1.1 Quartz Crystal Microbalance with Dissipation (QCM-D)

QCM is a technique that is used for monitoring of thin-film deposition and characterization of thin films [13]. QCM-D measures the frequency shifts and the dissipation of energy over a quartz crystal. A QCM sensor is a thin quartz crystal disk placed between two electrodes. Quartz is a piezoelectrical material, i.e., it has the property of undergoing mechanical deformation in the presence of an electric field. By applying a voltage between the two electrodes, the quartz disk will change its shape. These discs are cut in such a way that the deformation they go through is alongside the thickness, i.e., parallel to the surface of the discs. Therefore, if an oscillating voltage is applied to the quartz sensor, the sensor will oscillate back and forth according to the voltage.

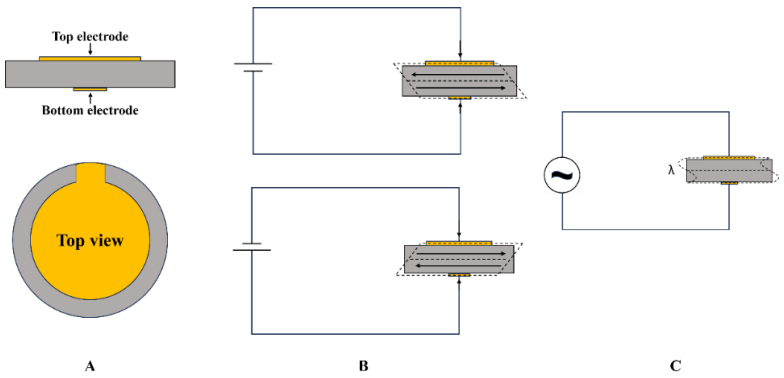

Figure 3: A) Top and side views of a QCM sensor. B) QCM sensor undergoing mechanical deformation under the application of a voltage. C) The same sensor undergoing mechanical deformation when an oscillating voltage is applied. [13].

The crystal has a resonance frequency, f_0. The frequency is related with the thickness of the disk, the wavelength of the oscillating voltage, the speed of sound in quartz and the overtone number by the following equation [14].

$$f_0 = \frac{v_q}{\lambda} = \frac{v_q}{2h} \tag{9}$$

Where h is the thickness of the disk, λ is the wavelength, v_q is the speed of sound in the quartz and n is the overtone number.

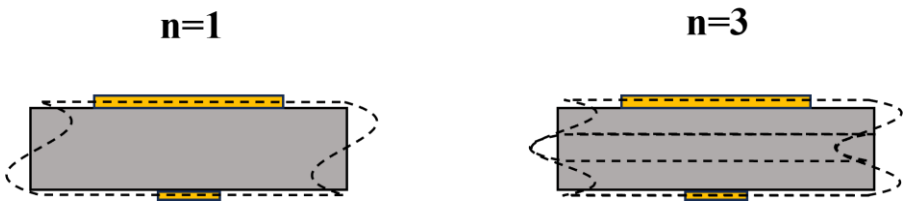

Figure 4: Close up of a cross section of a QCM sensor. The left sensor is resonating at the fundamental frequency, n=1, while the one at the right is n=3. [13].

The resonant frequency (f) can be defined as:

$$f = n \cdot \frac{v_q}{2h} = n \cdot f_0 \tag{10}$$

Other quantity that is important to define is the mass per unit area, expressed as:

$$\frac{M}{A} = m_q = 2h \cdot \rho_q \tag{11}$$

Where ρ_q is the density of the quartz. These two equations can be combined and derived, leading to:

$$df = -\frac{f}{m_q} dm_q \tag{12}$$

By making the approximation $df \rightarrow \Delta f$, this leads to the following equation:

$$df = \Delta f = -\frac{f}{2h \cdot \rho_q}\Delta m = -n\frac{f_0^2}{v_q \cdot \rho_q}\Delta m = -n\,\frac{1}{C}\,\Delta m \qquad (13)$$

Where C is called the sensitivity constant. For a 5 MHz crystal, the value of this constant is 17.7 ng/(Hz cm^2) [14]. Solving the previous equation for Δm, we obtain:

$$\Delta m = -C\,\frac{\Delta f}{n} \qquad (14)$$

Equation (14) is called the Sauerbrey Equation [15]. This equation establishes a relationship between the frequency shifts and the change of mass in the surface of the crystal.

The dissipation in the QCM, also referred to as energy dissipation, refers to the energy that is lost in the system during the experiment. This dissipation may be caused by several reasons [16], therefore it provides important information of the material deposited in the quartz sensor. To know if the Sauerbrey equation can be used or not, information regarding the energy loss needs to be known.

1.2 Small/Wide Angle X-ray Scattering (SAXS/WAXS)

X-rays are electromagnetic waves, with a wavelength in the order of 0.5–2.5 Å [17]. Scattering by x-rays occurs when an incident x-ray beam hits a target located at a distance *d* from the source of the x-rays, in an elastic collision. The scattered rays reach a detector at an angle 2θ placed at the same distance *d* from the target.

The intensity (*I*) of an X-ray beam is defined as the flow of energy per unit area per time. The intensity can also be defined as the square of the amplitude of the incident wave [18]. Considering the case in which the incident wave is a complex number, the intensity can be expressed as:

$$I = A^2 = AA^* \tag{15}$$

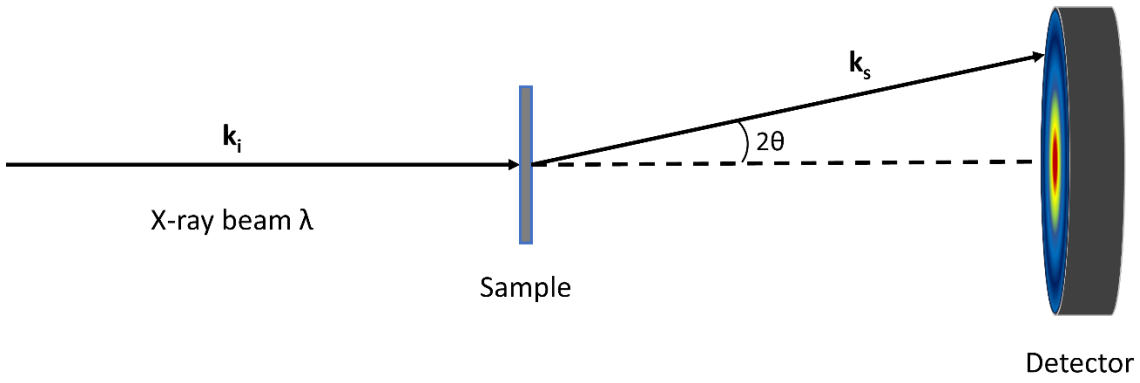

Figure 5: Representation of X-ray scattering geometry [19].

The intensities of x-ray scattering are plotted with respect to the magnitude of a new variable called the scattering wavevector ($\boldsymbol{q}$), defined as:

$$\boldsymbol{q} = \boldsymbol{k_s} - \boldsymbol{k_i} = \frac{2\pi \boldsymbol{S_s}}{\lambda} - \frac{2\pi \boldsymbol{S_i}}{\lambda} \tag{16}$$

Where $\boldsymbol{k_i}$ and $\boldsymbol{k_s}$ represent the incident and scattered wave vectors of the beam, respectively; $\boldsymbol{S_i}$ and $\boldsymbol{S_s}$ represent the respective traveling directions of $\boldsymbol{k_i}$ and $\boldsymbol{k_s}$. The magnitude of this vector, q, can be rewritten as [20]:

$$q = \frac{4\pi}{\lambda} \sin\theta \tag{17}$$

Where λ is the wavelength of the x-ray beam and θ the glancing angle. The relationship between the wavelength, θ and the lattice spacing (d) is given by Bragg's Law [21]:

$$2d \sin\theta = n\lambda \tag{18}$$

Where n is a positive integer.

Small-angle x-ray scattering (SAXS) is a technique used to analyze particles or structures in the order of 10 Å-1000 Å. The angles at which this technique is caried out are in the range of $2\theta < 5^{\circ}$ [18].

The intensity can be expressed in terms of the scattering vector. First, is considered the case in which x-rays are scattered by individual particles in one dimension. Each electron in the sample will generate a secondary wave once the incoming beam hits it. This wave has the general form $ae^{i\phi}$. Where a is the amplitude of the wave and ϕ is its phase. The total amplitude of the wave generated by all electrons in the sample is the sum of all individual secondary waves:

$$A = \sum_{k} a_k e^{i\phi_k} \tag{19}$$

In a three-dimensional case, and considering a large number of electrons, the sum is replaced by an integral and the intensity can be expressed as [22], [23], [24]:

$$I(q) = \left| \iiint e^{i\boldsymbol{q}\cdot\boldsymbol{r}} \rho(\boldsymbol{r}) dr \right|^2 \tag{20}$$

Where $\rho(\boldsymbol{r})$ is the electron density distribution of the material and $\mathbf{r}$ is the vector normal to the plane of the scattered wave [21]. This is an important equation given that with it we can obtain the values of the intensity for a specific interval of $\boldsymbol{q}$, also called the form factor of the particle [20], [23]. As the name suggests, the form factor provides an idea of the particle's shape and size. This equation can also be rewritten as follows:

$$I(q) = cP(q)\rho^2V^2 \quad (21)$$

Where $P(q)$ is the form factor, V is the particle volume and ρ is its density, and c the particle concentration. This equation, however, only considers the intensity of just one particle. Then equation (21) needs to be modified in order to include information regarding the contribution to the intensity by a set of particles, a structure factor. This modification leads to express equation (21) as:

$$I(q) = P(q)S(q)\rho^2V^2c \quad (22)$$

In which $S(q)$ is the structure factor and c is the concentration of the solution. With equation (22) we can obtain information regarding: (1) the particle's shape, and (2) the spatial correlations resulting from interactions between a set of particles. The intensities are collected from the raw data in the experiment and after finding proper mathematical models that fit the data, explicit, or approximate, functions for both $P(q)$ and $S(q)$ can be obtained.

2. Experimental Methods

2.1 Sample Preparation

2.1.1 Pulsed Laser Deposition

Thin films of MgO were deposited over the surface of a QCM sensor using pulsed laser deposition (PLD) at the Center for Nanophases Material Sciences (CNMS) at Oak Ridge National Laboratory (ORNL). The sensor was placed in sample holder facing downwards (see Figures 7 and 8) inside of a vacuum chamber at 24 ˚C while O_2 was pumped into the chamber with a flow rate of 10 standard cubic centimeter per minute (SCCM), at a pressure of 50 mTorr where a laser beam hit a 1-inch-diameter MgO target which was placed beneath the sensor. The pulse frequency of the laser was 10 Hz, with a wavelength of 248 nm, its energy density was 2 J/cm^2. With an estimated deposition rate of 0.09 Å per shot and a total of 10,000 shots, the final thickness of the MgO layer deposited in the crystal was estimated to be 900 Å = 90 nm.

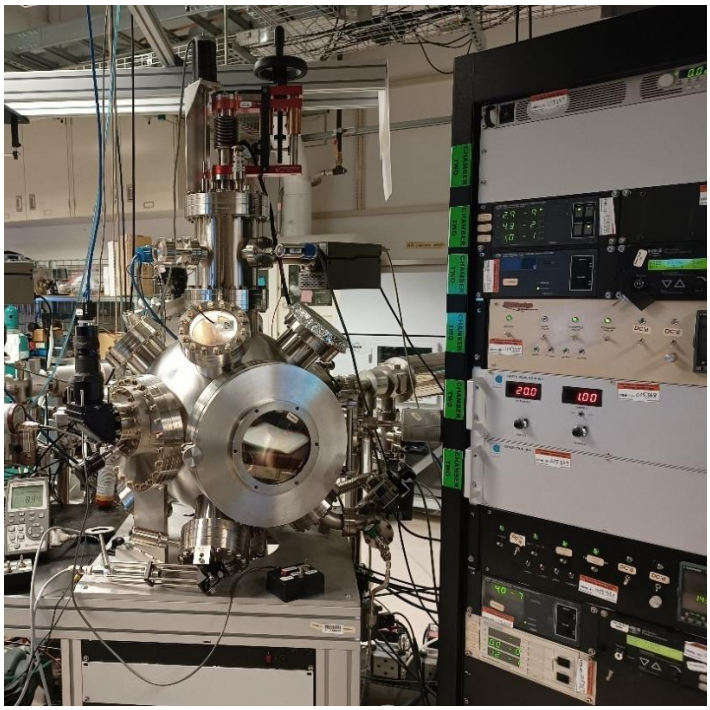

Figure 6: Vacuum chamber where thin film deposition using PLD was carried out.

Figure 7: Close view of the vacuum chamber. The structure at the top is the sample holder for the quartz sensor. The MgO target is located right beneath the ring-shaped structure held by a piston.

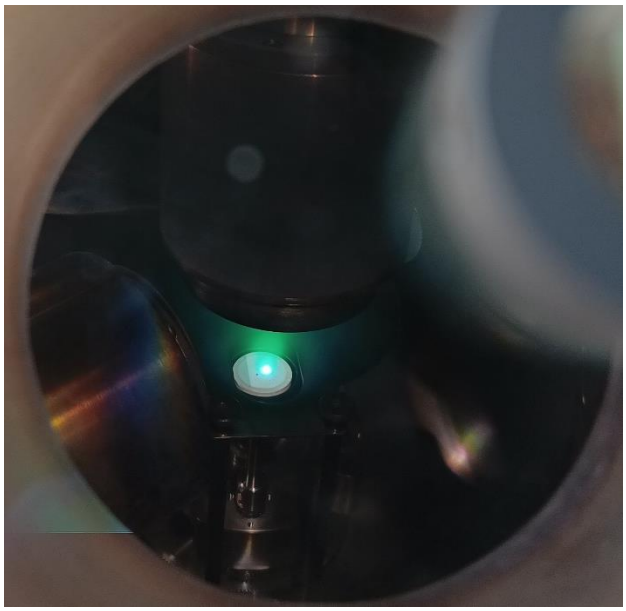

Figure 8: A different view inside the vacuum chamber at the moment at which the MgO target is hit by the laser during the PLD experiment. The dark cylinder-shaped structure right above the target is where the QCM sensor is located.

2.1.2. QCM-D

QCM-D analysis was conducted using a QSense Pro (figure 9) instrument [25] at CNMS, ORNL. The quartz sensors were positioned in a sample holder called the QSense Pro Flow Module (Figure 10) and then placed inside the QSense Pro's Work Area. To investigate how the formation of brucite on the sensor surface impacts its mass, ultra-pure deionized water equilibrated to atmosphere (pH: 5.76) was introduced into flasks and flowed at a rate of 20 µl/min. These experiments were carried out at: 25 °C, 40 °C, with durations of 29 h, 15 h, and 8.7 h, respectively.

Figure 9: QSense Pro instrument [25].

Figure 10: QSense Pro Flow Module.

2.1.3. Batch Experiments

Batch experiments were conducted in order to analyze how brucite forms over the surface of different MgO powders at different static relative humidity (RH) levels over time. Three different types of MgO powders were used for these experiments: Alpha Aesar® (AA), Beantown Chemical® (BTC) and Sky Spring® (SS). With each one of these powders having a different surface area: AA (6 m^2/g), BTC (31 m^2/g) and SS (19 m^2/g). Small amounts of these powders each were exposed at 6 different relative humidities: 11%, 23%, 53%, 75%, 85% and 100%. Saturated aqueous solutions were employed to replicate the RH levels previously mentioned [26]. These samples were exposed for durations of 1 day, 2 days, 1 week, 2 weeks, 1 month and 2 months.

The first step involved preparing a total of 108 vials for depositing the powders. To minimize errors, the mass of each vial was meticulously measured. The mass values, along with the amounts of powder deposited in each vial, are documented in the Appendix section tables.

The second step was the preparation of the MgO powders. 15 grams of each powder were put in separate ceramic crucibles. The materials were heated at 450 °C for 3 hours. The instrument used was an MTI Corporation® KSL-1100X-S-UL-LD furnace. Argon (Ar) gas flowed at a rate of 20 milliliters normal per minute (mln/min) into the furnace to avoid the formation of carbonates due to atmospheric CO_2.

Figure 11: Ceramic crucibles containing the MgO powders before the heating process.

The preparation of the saturated solutions involved mixing 12 grams of deionized (DI) water with the respective amount of each salt inside plastic containers. Since each salt required a different quantity of material, we measured their masses beforehand. The following table displays the salts used in the solutions, their relative humidity levels, and the masses of water and salt added:

Table 1: Masses of each salt and the water added.

Material [chemical formula]	**RH (%)**	**Water Added (g)**	**Salt Added (g)**
Lithium Chloride [LiCl]	11	12.0332	10.6478
Potassium Acetate [$C_2H_3KO_3$]	23	12.057	33.921
Magnesium Nitrate Hexahydrate [$(Mg(NO_3)_2)\cdot 6\ H_2O$]	53	12.0573	32.3738
Sodium Chloride [NaCl]	75	12.0765	4.5326
Potassium Chloride [KCl]	85	12.0765	4.4888
Water [H_2O]	100	12.001	0

The mixing process was straightforward: we added the solute, closed the vial with a cap, and shook it. For each solution, 3 ml were deposited inside the container using a transfer pipette (due to the volume increase). However, for potassium acetate and magnesium nitrate, which expanded almost 5 times their original space, we used 8-9 ml. Finally, the 100% relative humidity (RH) container was filled with 5 ml of DI water.

The vials were grouped in threes, each containing a specific type of powder, and placed into bottles corresponding to a specific relative humidity level. After these bottles were closed, the lids were closed with black tape to reduce the possibility of water vapor leakage.

Figure 12: Different MgO powders exposed at the same RH level for a specific exposure time.

After the samples were exposed for the determined time, we measured their masses. Subsequently, the vials were placed in an oven under vacuum at 120 °C for 24 hours to remove any physically adsorbed water. Once the drying process was complete, we measured the mass of the samples again.

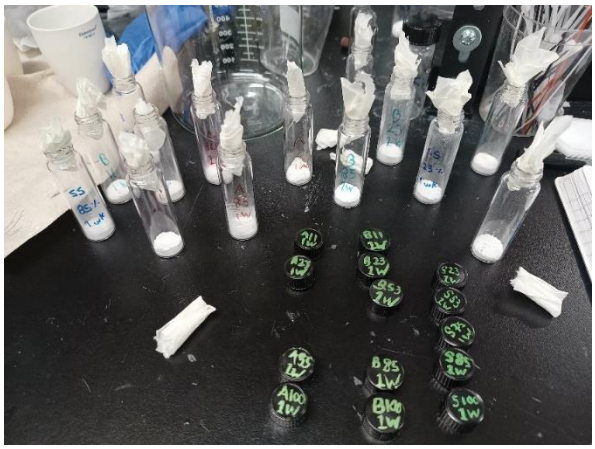

Figure 13:Vials with different MgO powders after the heating process.

The following step focused on preparing Cole-Parmer® Kapton (polyimide) tubing to house the samples for subsequent analysis using SAXS and WAXS. These tubes have an inner diameter of

1.00584 mm. The tubing preparation process included cutting 15 mm-length sections. To seal the tube ends, we used copper (Cu) wiring (16 gauge). Specifically:

Set A: Consisted of 8 mm-length wires.

Set T: Comprised 20 mm-length wires.

We sealed one end of the Kapton tubes (K) with the A piece (as shown in Figure 16) by inserting the Cu wire into the Kapton at a distance of 5 mm. The other end was sealed with the T piece, maintaining a distance of 5 mm. The space between the two Cu wires (section where the letter K is shown in Figure 14) is where the sample is stored. The reason for this arrangement is to have all samples at the same height in the sample holder and thus make their analysis easier during SAXS and WAXS experiments.

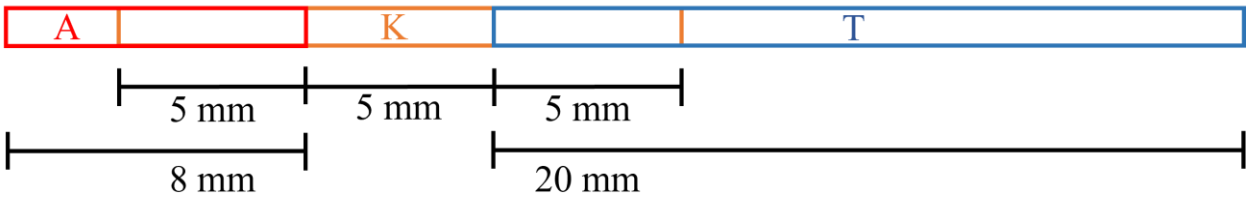

Figure 14: Schematic representation of the copper wires and Kapton tubes arrangement.

Figure 15: Materials used in the preparation of the sample tubes.

The following step is the addition of powder to the sample tube. The mass of the tube, both empty and with the powder added, was also measured. In order to ensure the material is well-packed, the tube was repeatedly tapped until the material was observed to stop compressing.

The final step in the preparation of the Kapton tubes involved the use of J-B Weld® epoxy (steel and hardener) to seal both ends outside where the Cu wire was inserted in the Kapton to ensure closed seal. After that, the sample tubes were allowed to dry for 24 hours.

Figure 16: Kapton tubes after being sealed. The tubes are separated by the type of powder used.

Once 24 hours passed, the sample tubes were placed in the sample holder.

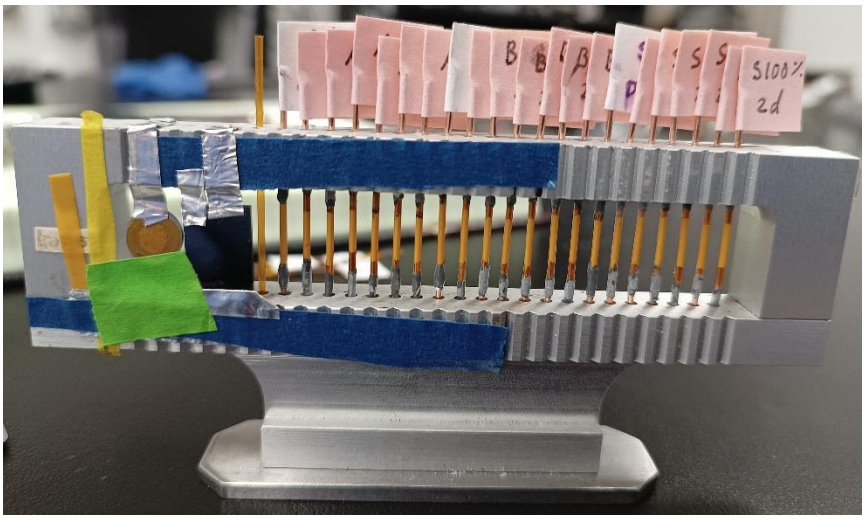

Figure 17: Sample holder for the SAXS/WAXS experiments.

Once the holder was loaded with the samples, it was placed inside the device used for the WAXS/SAXS experiments. The device utilized in these experiments was a XENOCS Xeuss 2.0 SAXS/WAXS instrument. These experiments involved placing the samples inside a vacuum chamber to enhance the quality of the data collected. Afterward, the samples were aligned, and their positions were measured to ensure that the X-rays would hit the samples and the scattering data would be accurately collected. For both experiments, a wavelength of 1.54 Å was used. The SAXS experiments lasted 3-4 hours each, and the WAXS ones lasted 10-12 hours each. Once the data was collected, the intensities of each sample and the raw data were gathered using Xenocs XSACT software.

Figure 18: XENOCSs Xeuss 2.0 SAXS/WAXS instrument.

3. Results

3.1 QCM-D

The raw data obtained for the two sets of experiments were analyzed using Origin 2022b. In both cases, the Sauerbrey equation was applied for the frequency shifts, and the following plots were obtained.

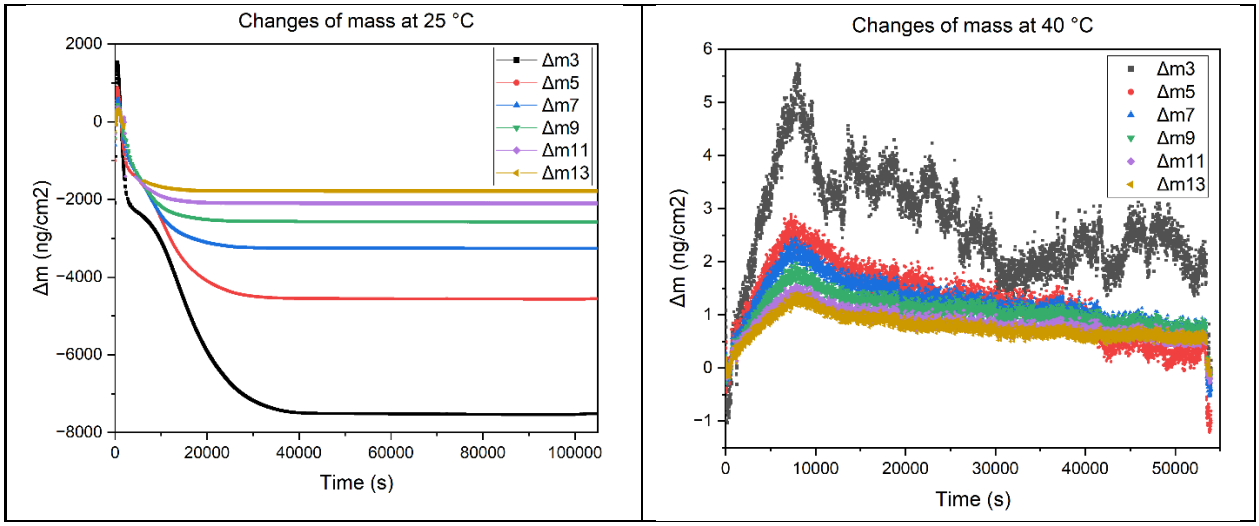

Figure 19: Change of mass for the QCM-D experiments at 25 ˚C (left) and 40 ˚C (right).

3.2 SAXS/WAXS

The raw data obtained from the experiments were reduced, that is, any contribution to the scattering generated by the Kapton tubes was removed, and the intensities were normalized with respect to the thickness of the sample tube. By performing this process, the raw data are transformed into a scattering intensity profile that will be used for further analysis. The subsequent figures contain the plots for all experiments after reduction. These figures are divided into two major groups, according to the type of experiment. Similarly, each group is divided into three subgroups, one for each type of powder. Finally, all plots are organized in ascending order with respect to the exposure time.

3.2.1 SAXS

3.2.1.1 Alpha Aesar (AA)

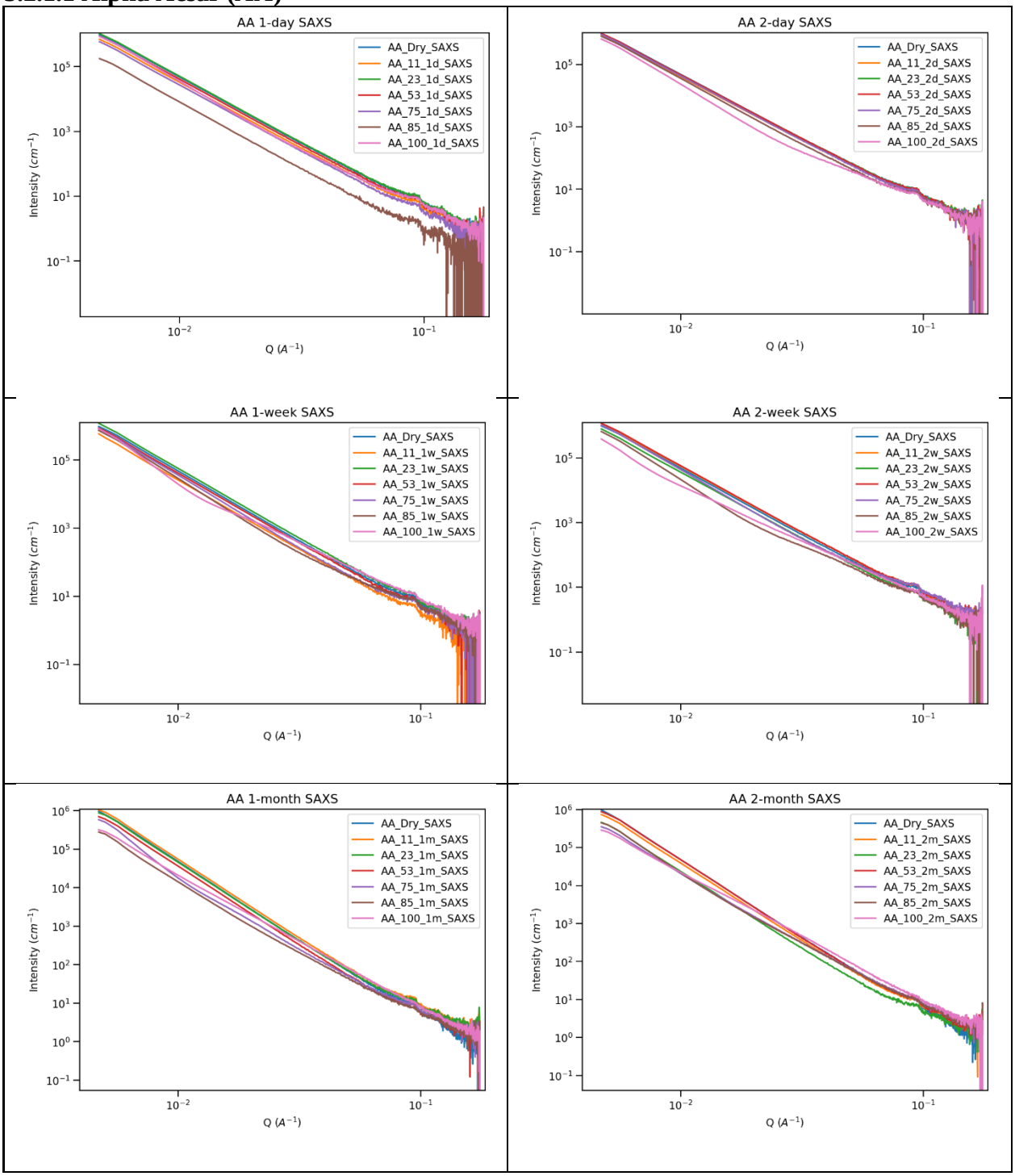

Figure 20: Intensities of the AA powder at different exposure times.

3.2.1.2 Beantown Chemical (BTC)

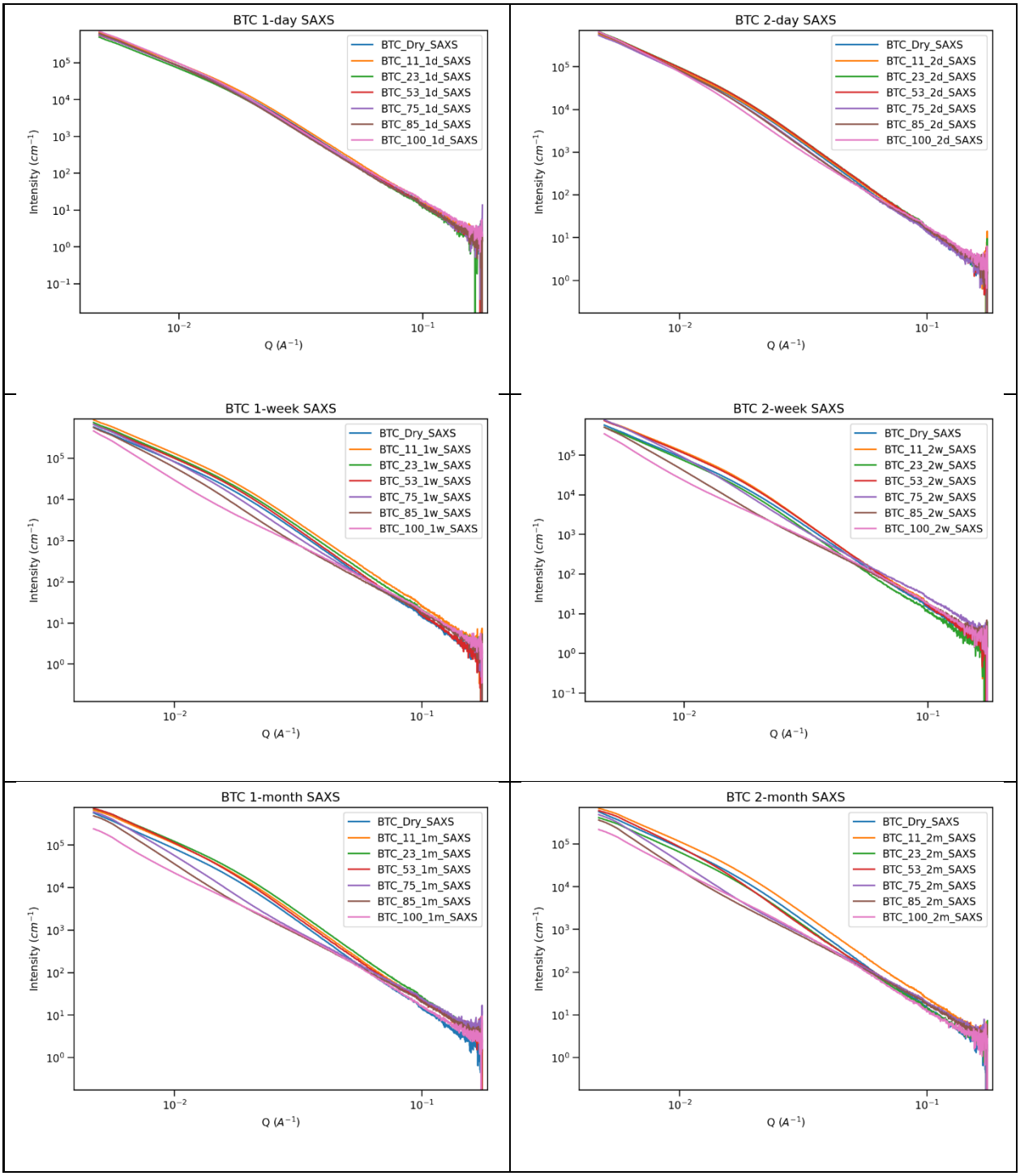

Figure 21: Intensities of the BTC powder at different exposure times.

2.2.1.3 Sky Spring (SS)

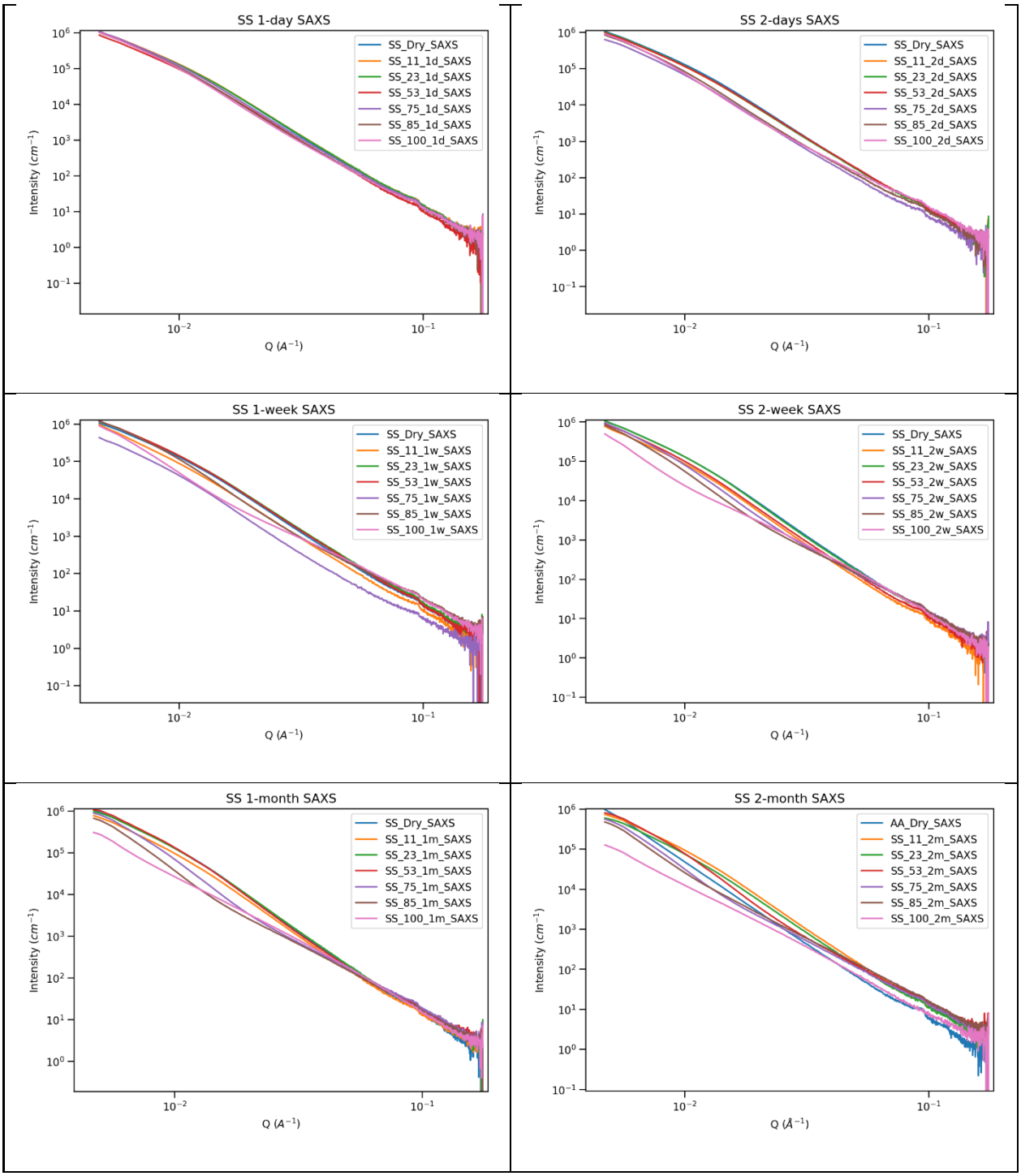

Figure 22: Intensities of the SS powder at different exposure times.

3.2.2 WAXS

3.2.2.1 Alpha Aesar (AA)

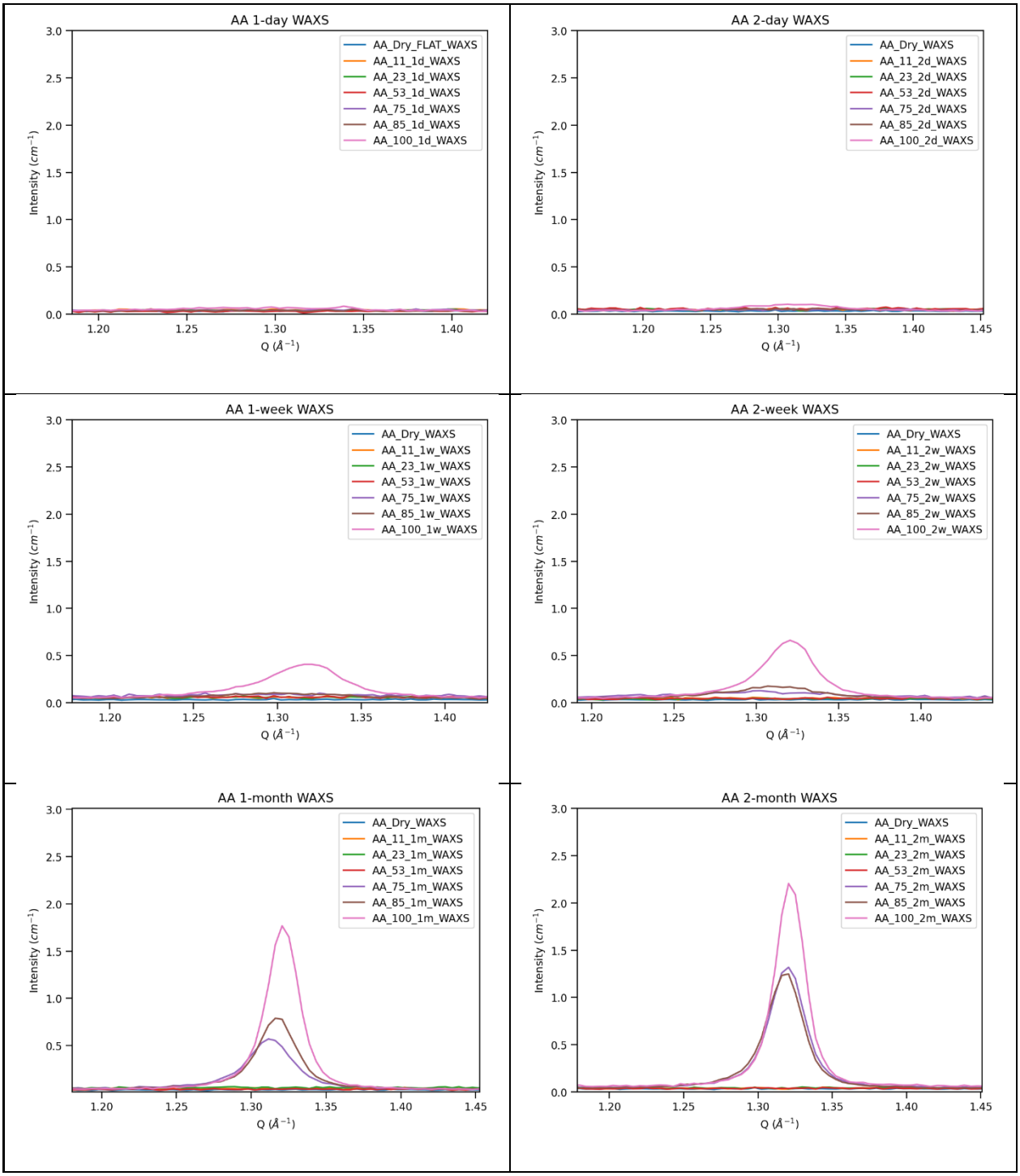

Figure 23: Intensities of the AA powder at different exposure times. After 1-week exposure time, peaks for the three highest relative humidity levels began to arise. No peaks were observed of the three lowest RH levels.

3.2.2.2 Beantown Chemical (BTC)

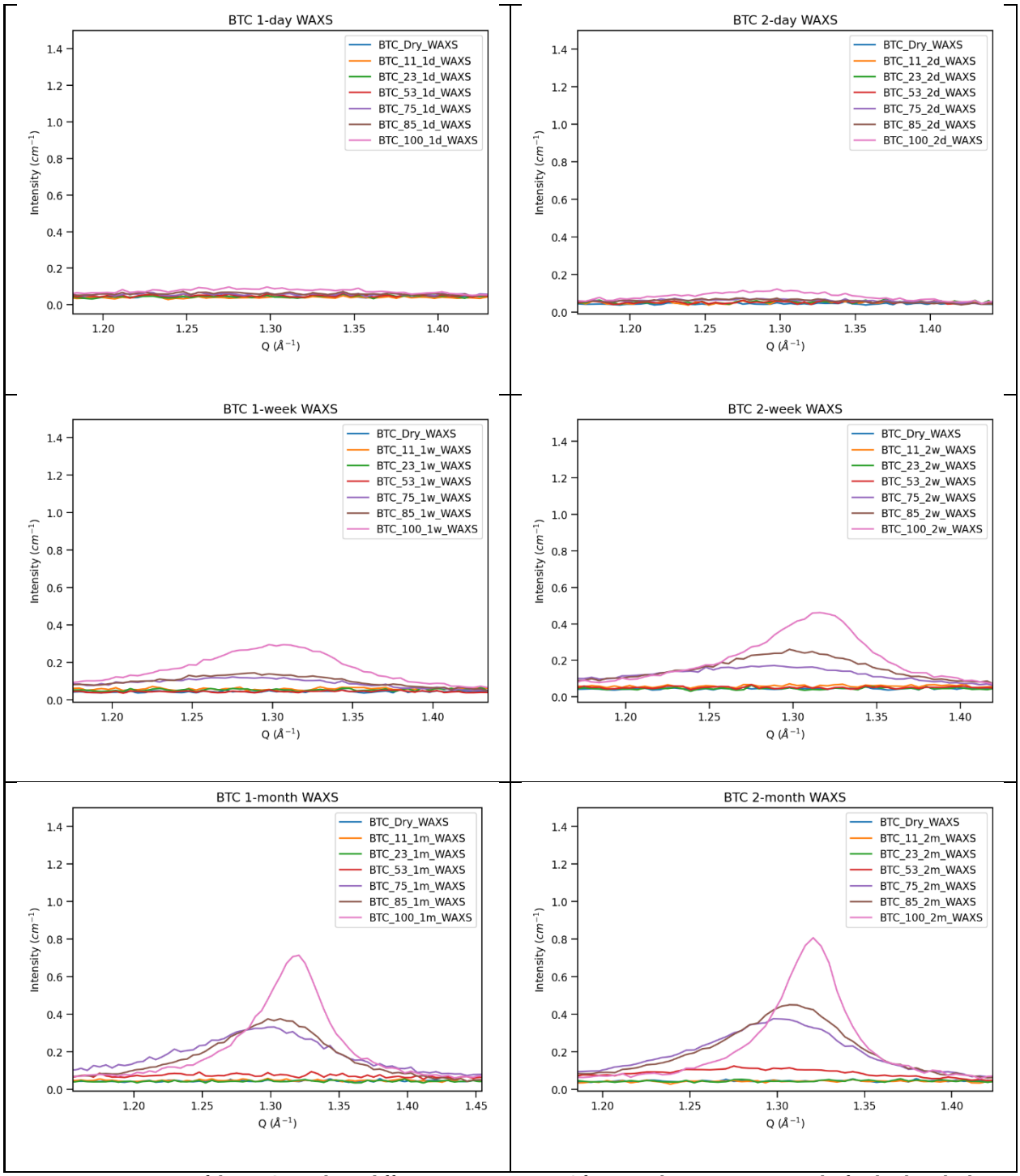

Figure 24: Intensities of the BTC powder at different exposure times. After 1-week exposure time, peaks for the three highest relative humidity levels began to arise. No peaks were observed of the three lowest RH levels.

3.2.2.3 Sky Spring (SS)

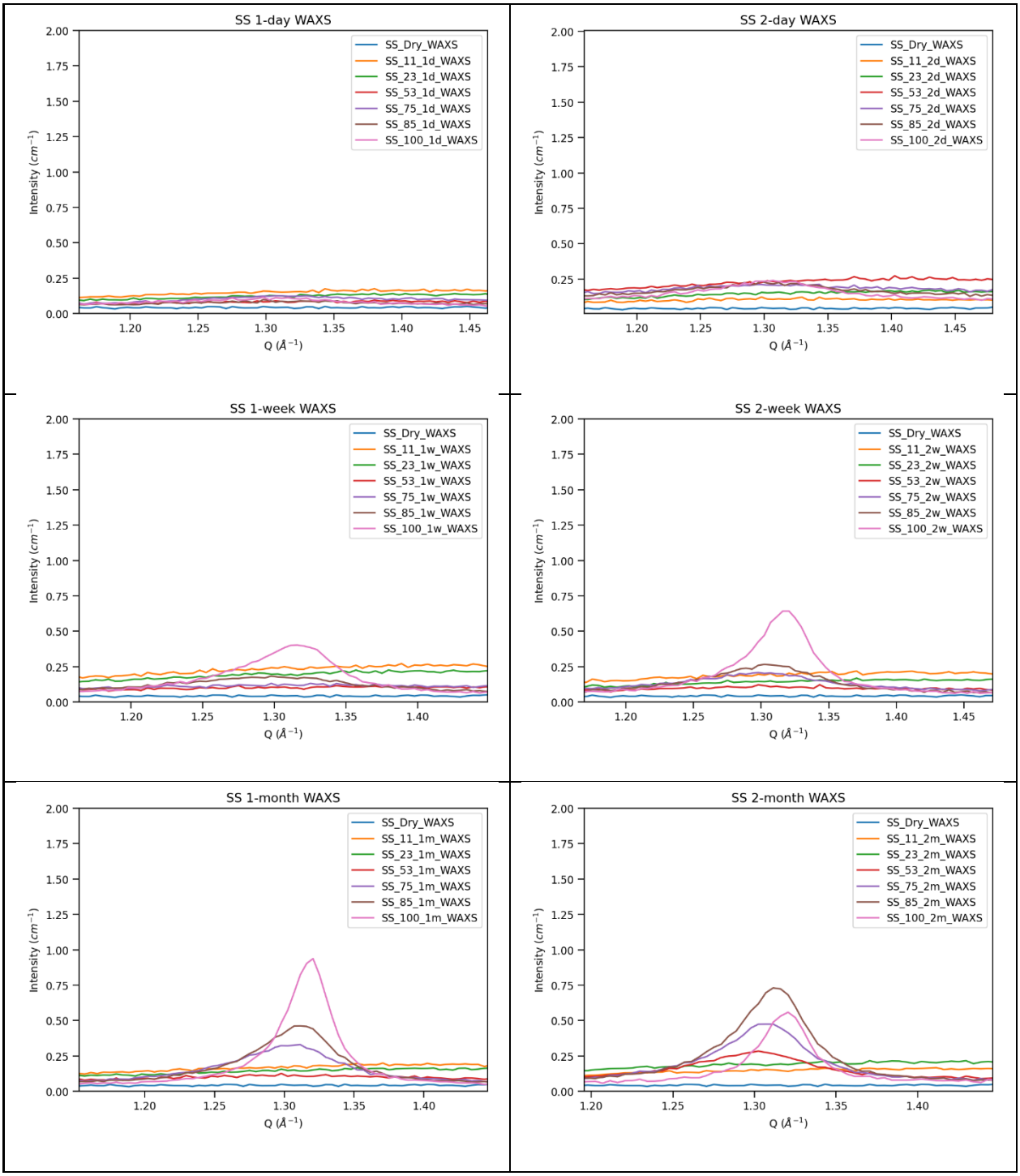

Figure 25: Intensities of the SS powder at different exposure times. After 1-week exposure time, peaks for the three highest relative humidity levels began to arise. No peaks were observed of the three lowest RH levels.

3.3 Changes of Mass of the powders

The masses of each vial used in the experiment, the mass of the MgO added to each vial, and the mass of the vials after RH exposure and after being heated in the furnace under vacuum at 120°C for 24 hours were measured. With this information, we determined the mass increase after RH exposure and the proportions of water and brucite. The tables containing all recorded measurements are in the appendix section. These measurements were performed for each type of powder used in this work at all exposure times. The plots of the changes of mass for all powders are shown below.

3.3.1 Alpha Aesar (AA)

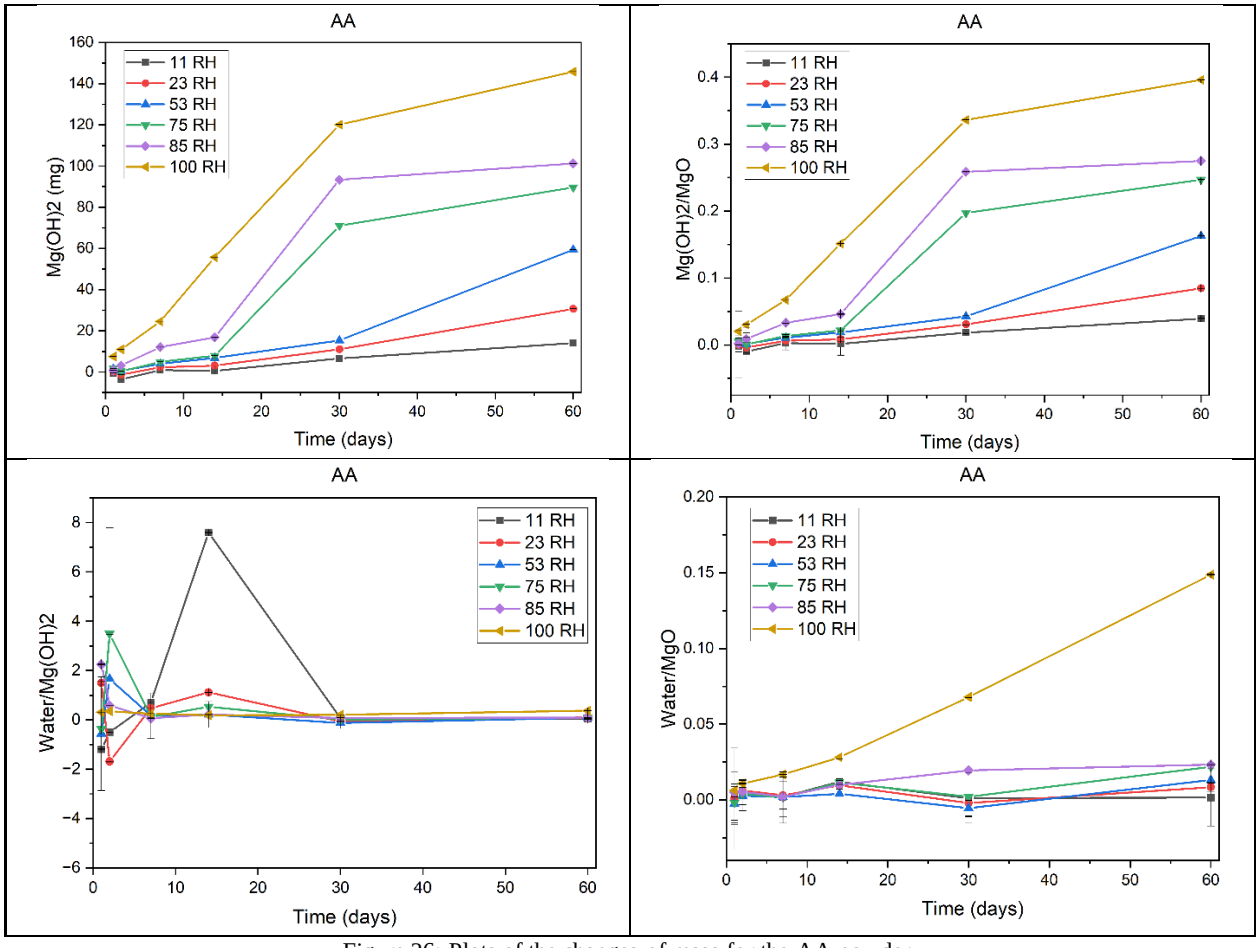

Figure 26: Plots of the changes of mass for the AA powder.

3.3.2 Beantown Chemical (BTC)

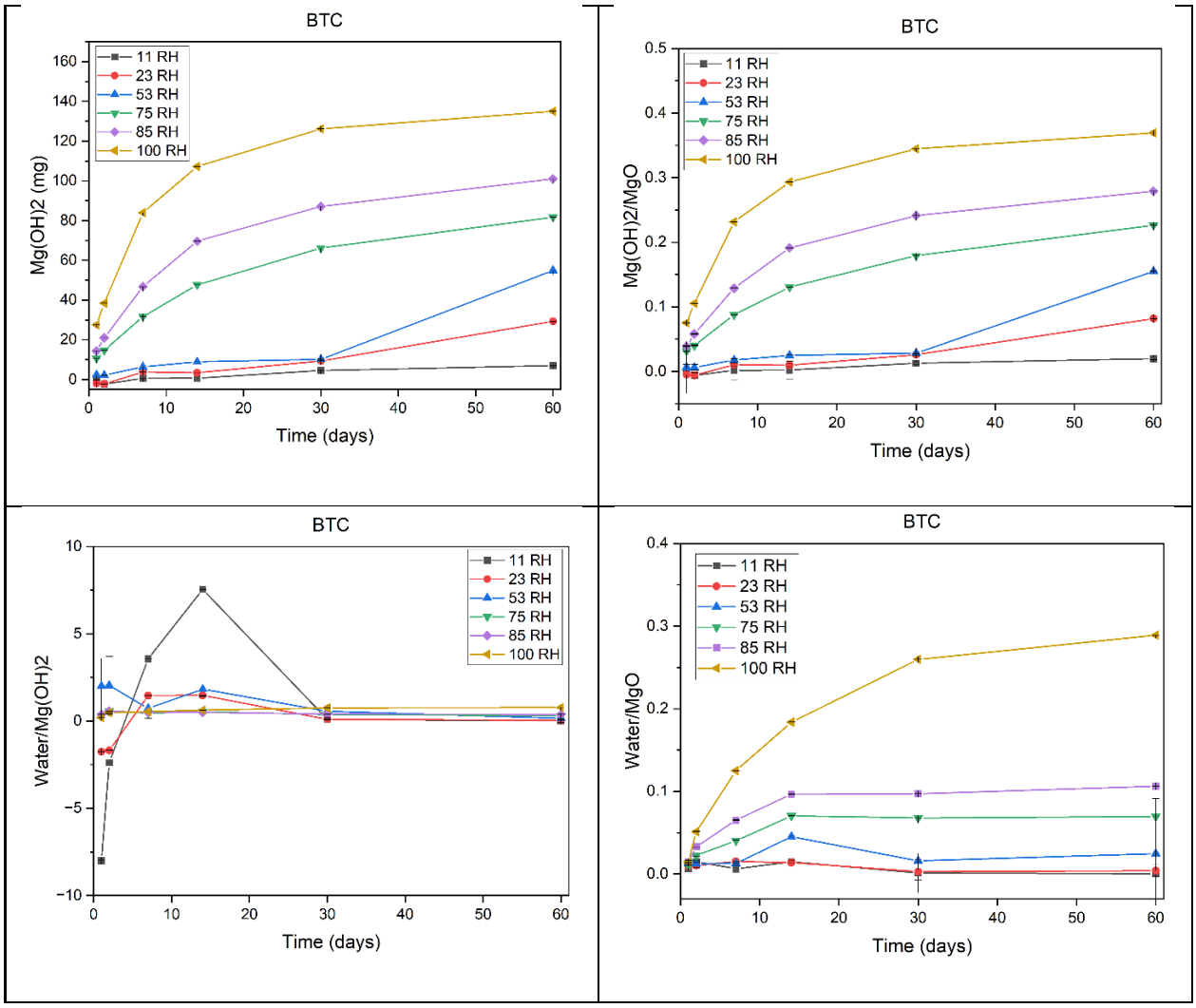

Figure 27: Plots of the changes of mass for the BTC powder.

3.3.3 Sky Springs (SS)

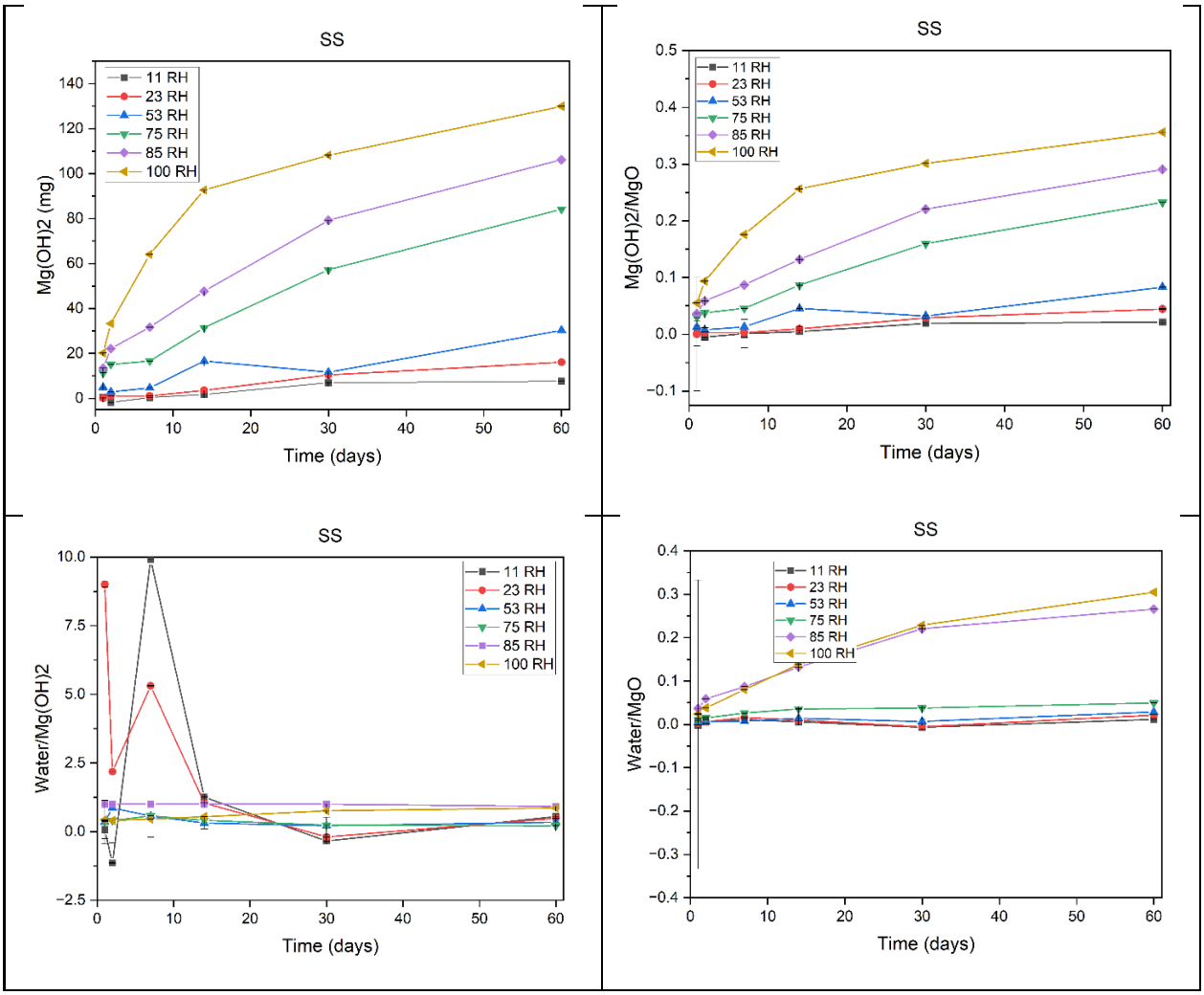

Figure 28: Plots of the changes of mass for the SS powder.

4. Analysis

4.1 QCM-D

In the experiment at 25 °C, two increases in mass were observed in the first 700 seconds for all overtones. The first one occurred 120 seconds after the experiment began, followed by a small decrease that lasted until 180 seconds. The second increase occurred after this time, reaching their maximum values around 551 seconds to 570 seconds. After this point, the changes in mass continuously decreased. In the region between 1100 seconds and 1350 seconds, the plots intersected with the others, and their order began to flip, with the plots corresponding to the first overtones exhibiting a faster decay compared to the plot corresponding to the subsequent overtone. In the region between 2000 seconds and 6500 seconds, data loss is evident as some gaps in the changes of mass began to appear, but the general trend in the plots is still apparent. In the region between 6500 seconds and 9000 seconds, some plots overlap; after this time, the plots exhibit the previous trend that they did after 1350 seconds. After 9000 seconds, the change of mass for a given overtone will present a faster decrease than that for the next overtone. After 40000 seconds, all plots began to flatten, showing no significant changes for the remainder of the experiment.

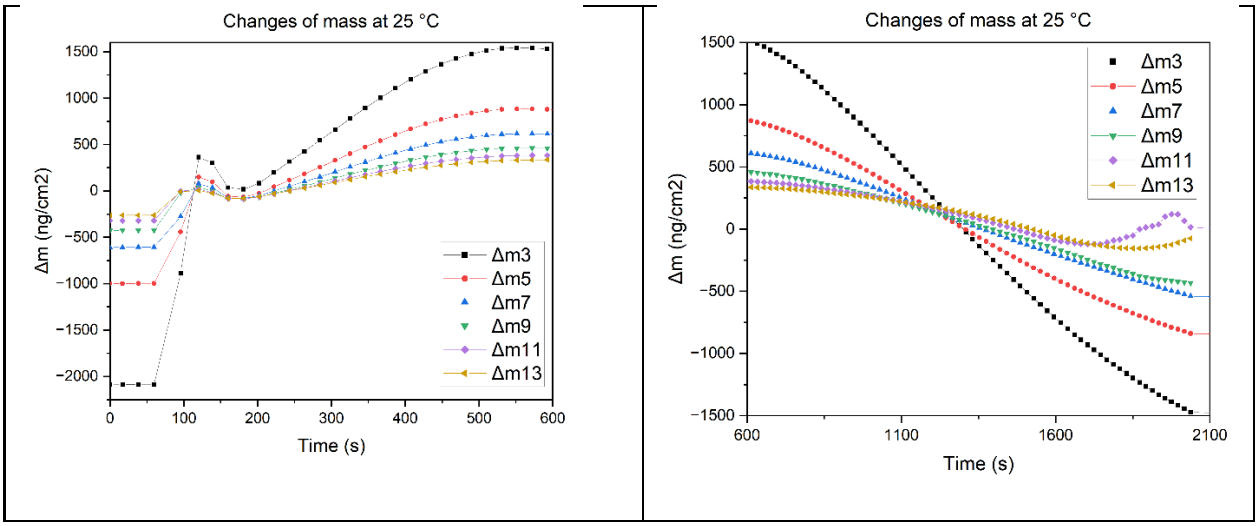

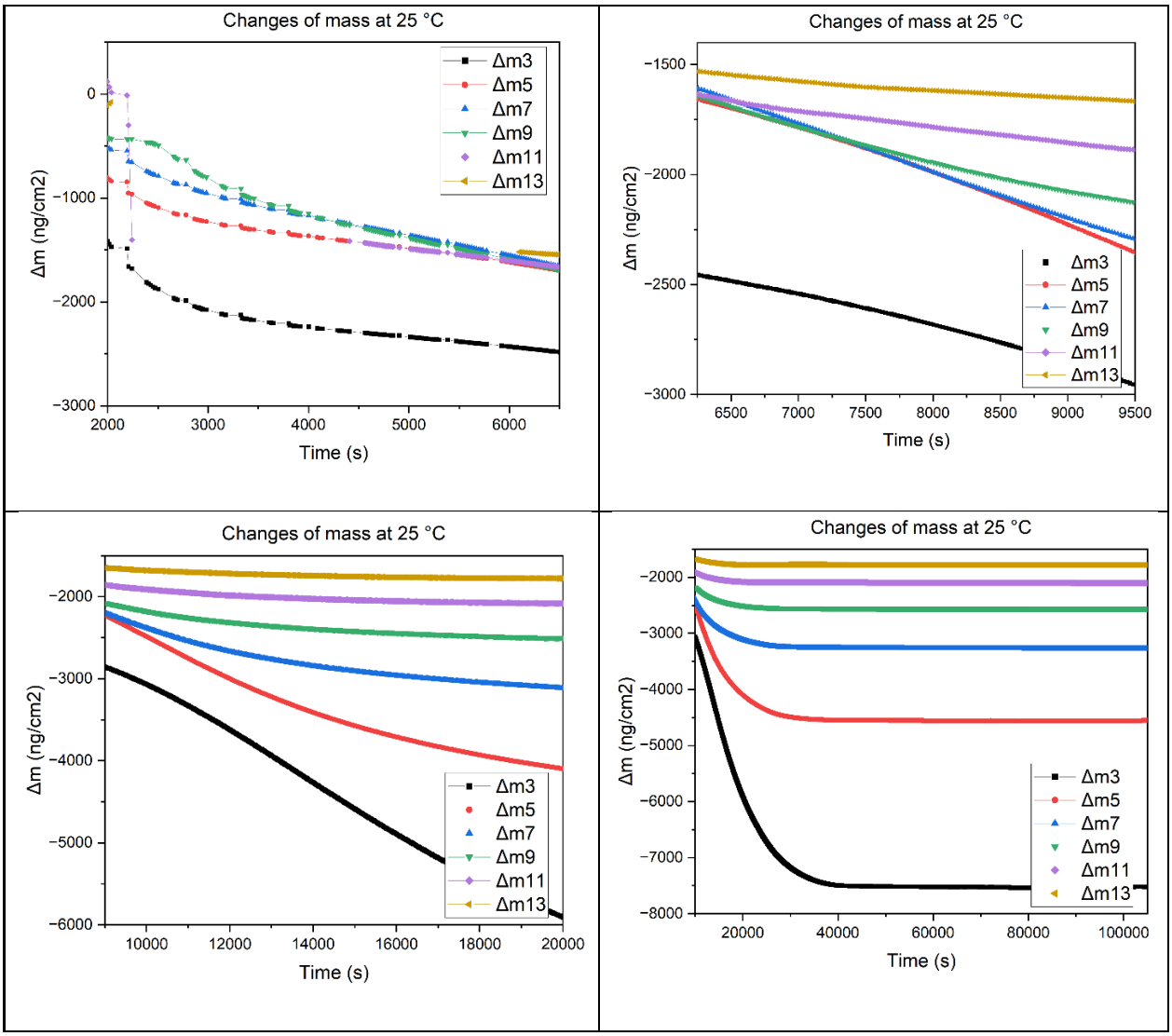

Figure 29: Different regions of the QCM experiment at 25 ˚C.

In the experiment at 40 ˚C, all changes of mass exhibited an increase since the beginning and reached their maximum after 8000 s. After this point, a decrease of mass was observed in all plots. In contrast with the previous experiment, the plots for the changes of mass for a given overtone have smaller values than the one for the previous overtone.

In both experiments, two regions—one per experiment—were identified in which the mass changes were positive for all overtones. For the experiment at 25 °C, this region is in the range of 170 s – 700 s. In the experiment at 40 °C, this region is in the range of 0 s – 8000 s.

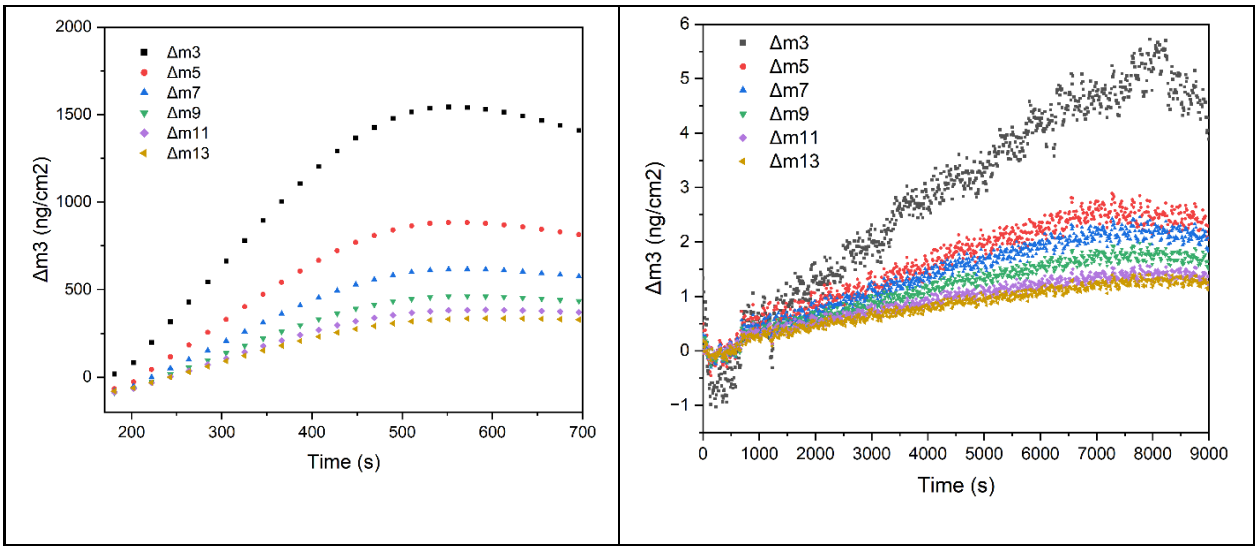

Figure 30: Regions where growth was observed in the QCM-D experiments at 25 C (left) and 40 C (right).

Data fitting in Origin 2022b was carried out to find relevant parameters in the brucite growth process. The model used to analyze the brucite growth rates is a modified version of the JMAK model [27].

$$M(t) = M_0(1 - \exp\left[-(\alpha(\mathrm{t} - \mathrm{t}_0))^d\right]) \qquad (23)$$

Where $M(t)$ is the change of mass per unit area [ng/cm^2], M_0 is the maximum change of mass per unit area [ng/cm^2], α is the rate constant [1/s], t_0 is the time at which nucleation/growth begins [s] and d is the dimensionality of growth.

4.1.1 Experiment at 25 ˚C

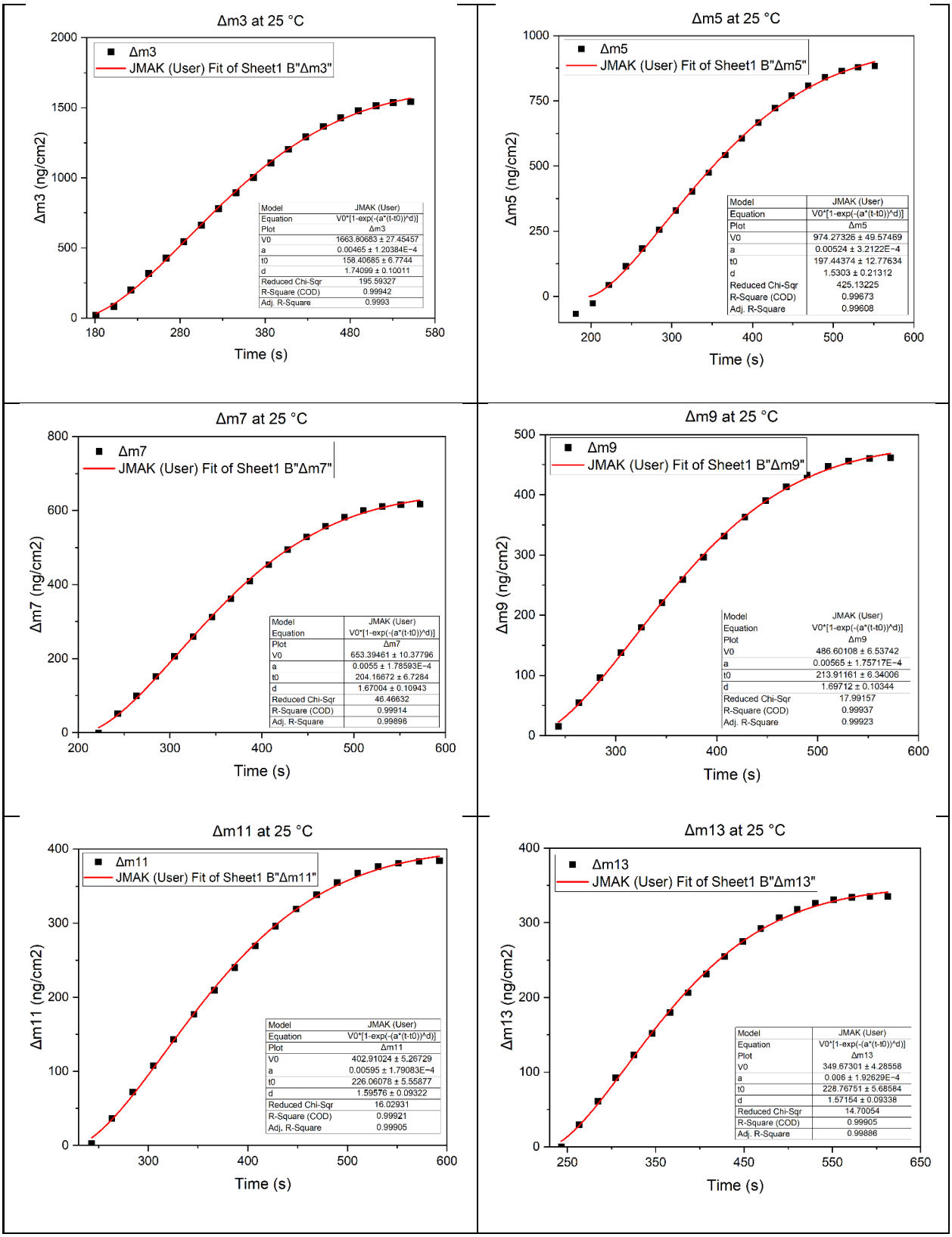

Figure 31: Data fitting for the experiment at 25 ˚C using the JMAK model.

Information containing the values of all parameters is displayed in the following table.

Table 2: Parameters of the experiment at 25 ˚C.

Parameters :	**M_0 (ng/cm^2)**	***a* (1/s)**	**t_0(s)**	***d***
Δm3	1663.80683 ± 27.45457	0.00465 ± 1.20384E-4	158.40685 ± 6.7744	1.74099 ± 0.10011
Δm5	974.27326 ± 49.57469	0.00524 ± 3.2122E-4	197.44374 ± 12.77634	1.5303 ± 0.21312
Δm7	653.39461 ± 10.37796	0.0055 ± 1.78593E-4	204.16672 ± 6.7284	1.67004 ± 0.10943
Δm9	486.60108 ± 6.53742	0.00565 ± 1.75717E-4	213.91161 ± 6.34006	1.69712 ± 0.10344
Δm11	402.91024 ± 5.26729	0.00595 ± 1.79083E-4	226.06078 ± 5.55877	1.59576 ± 0.09322
Δm13	349.67301 ± 4.28558	0.006 ± 1.92629E-4	228.76751 ± 5.68584	1.57154 ± 0.09338

4.1.2 Experiment at 40 ˚C

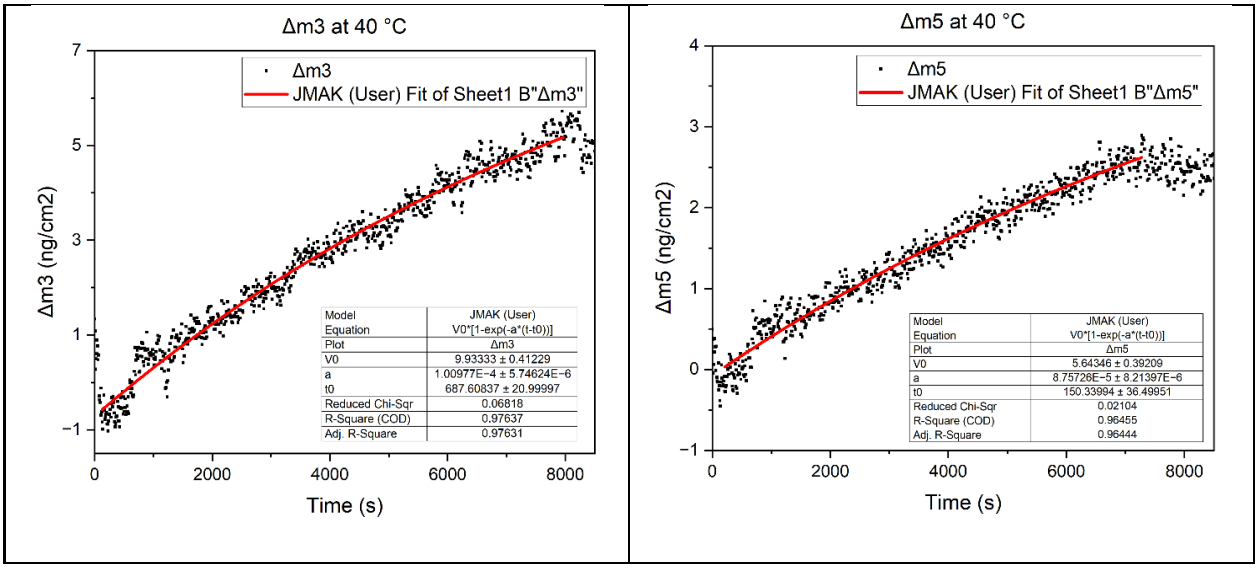

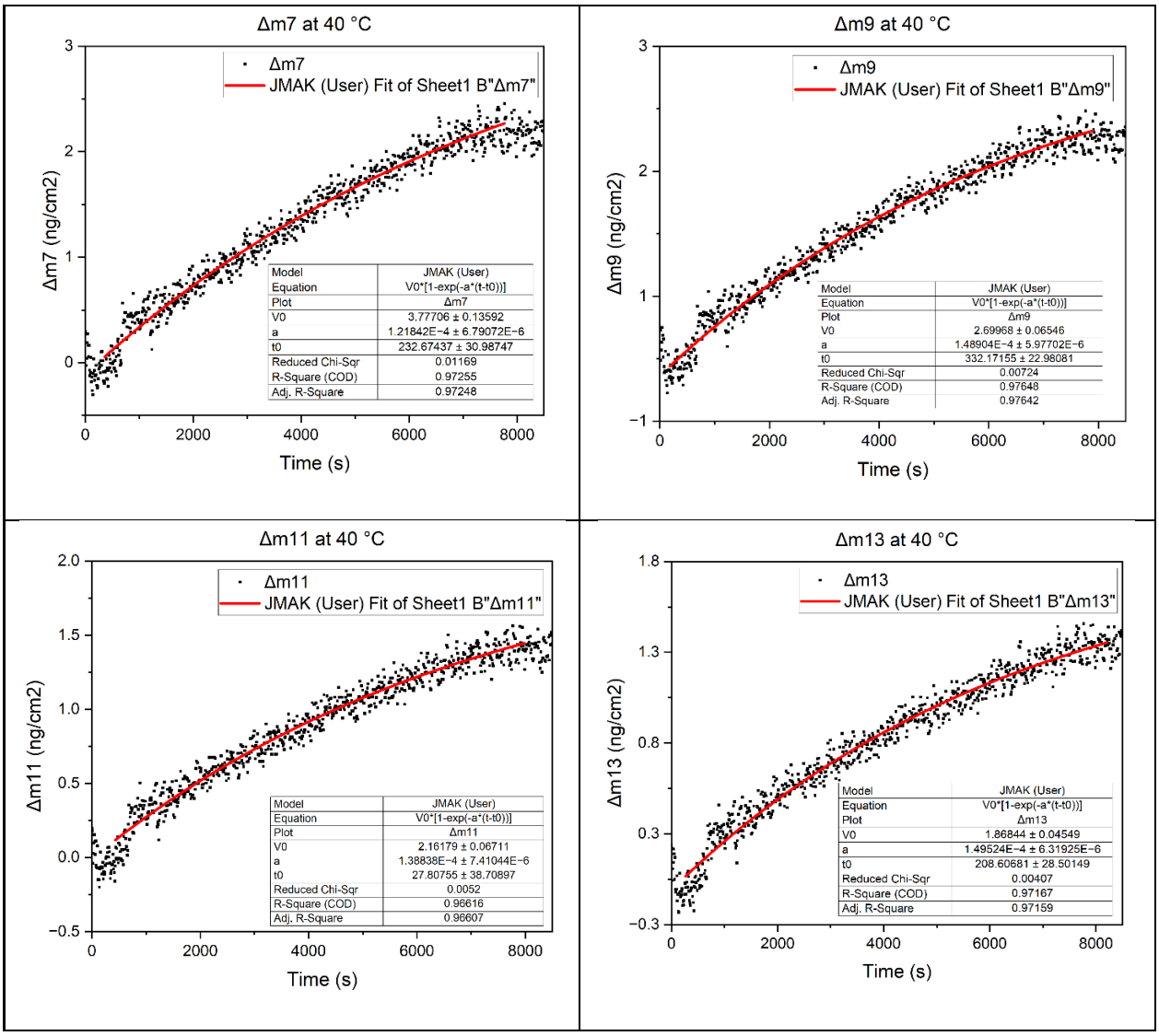

Figure 32: Data fitting for the experiment at 40 ˚C. In this analysis, the dimensionality of growth was set equal to 1.

Information containing the values of all parameters is displayed in the following table.

Table 3: Parameters of the experiment at 40 ˚C.

Parameters:	**M_0 (ng/cm^2)**	***a* (1/s)**	**t_0(s)**
Δm3	9.93333 ± 0.41229	1.00977E-4 ± 5.74624E-6	687.60837 ± 20.99997
Δm5	5.64346 ± 0.39209	8.75726E-5 ± 8.21397E-6	150.33994 ± 36.49951
Δm7	3.77706 ± 0.13592	1.21842E-4 ± 6.79072E-6	232.67437 ± 30.98747
Δm9	2.69968 ± 0.06546	1.48904E-4 ± 5.97702E-6	332.17155 ± 22.98081

Δm11	2.16179 ± 0.06711	1.38838E-4 ± 7.41044E-6	27.80755 ± 38.70897
Δm13	1.86844 ± 0.04549	1.49524E-4 ± 6.31925E-6	208.60681 ± 28.50149

4.2 SAXS/WAXS

4.2.1 Changes of mass of the powders

Data fitting using equation (23) on the plots for the $Mg(OH)_2$ and $Mg(OH)_2$/MgO growth obtained in Section 5.3 was also performed. Fitting of these graphs was conducted only on the plots with the three highest RH levels: 75%, 85%, and 100%.

4.2.1.1 Alpha Aesar (AA)

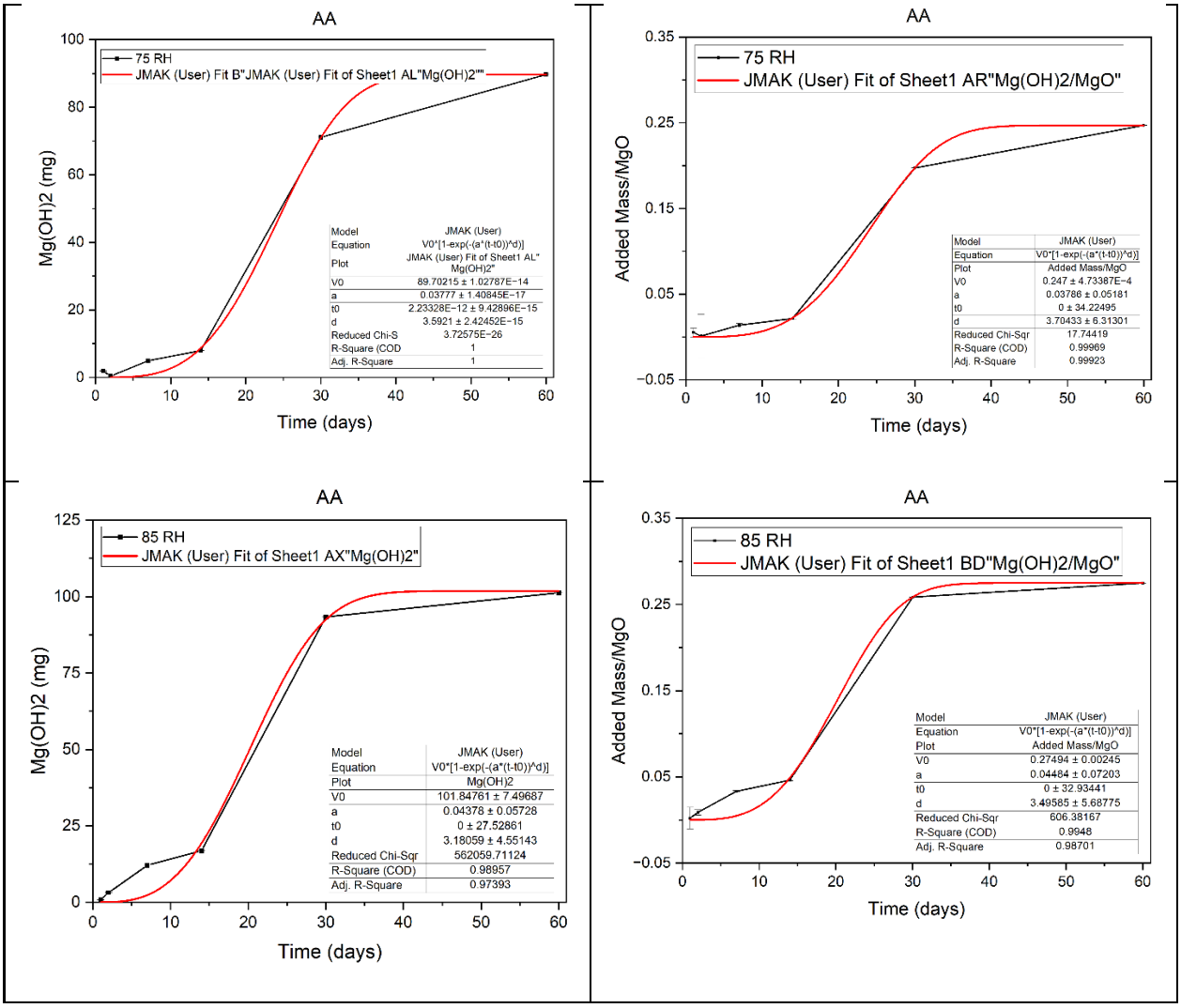

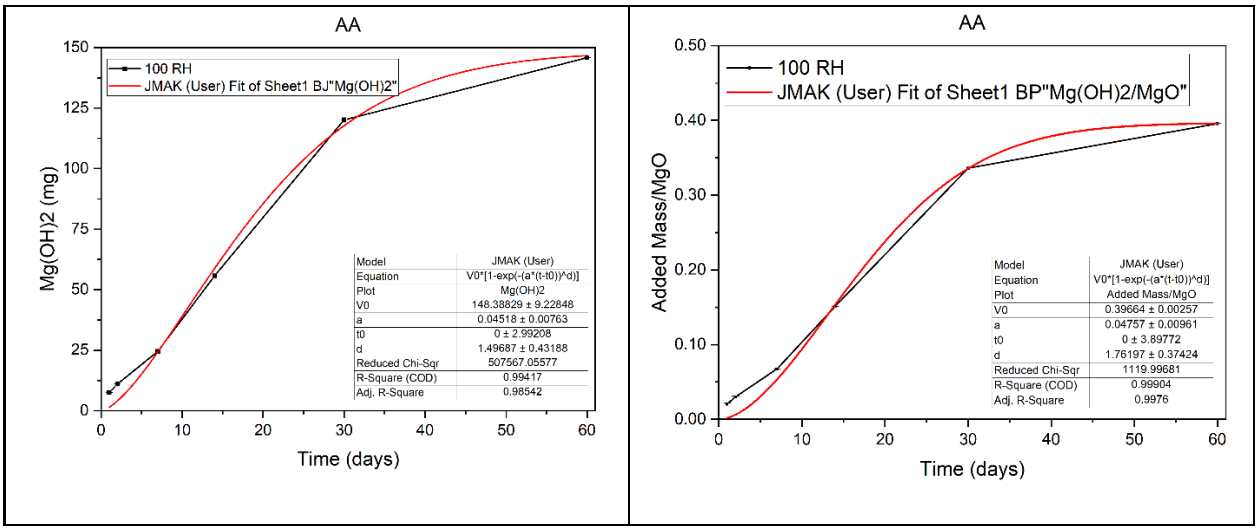

Figure 33: Data fitting for the AA powder at 75%, 85% and 100 % RH.

4.2.1.2 Beantown Chemical (BTC)

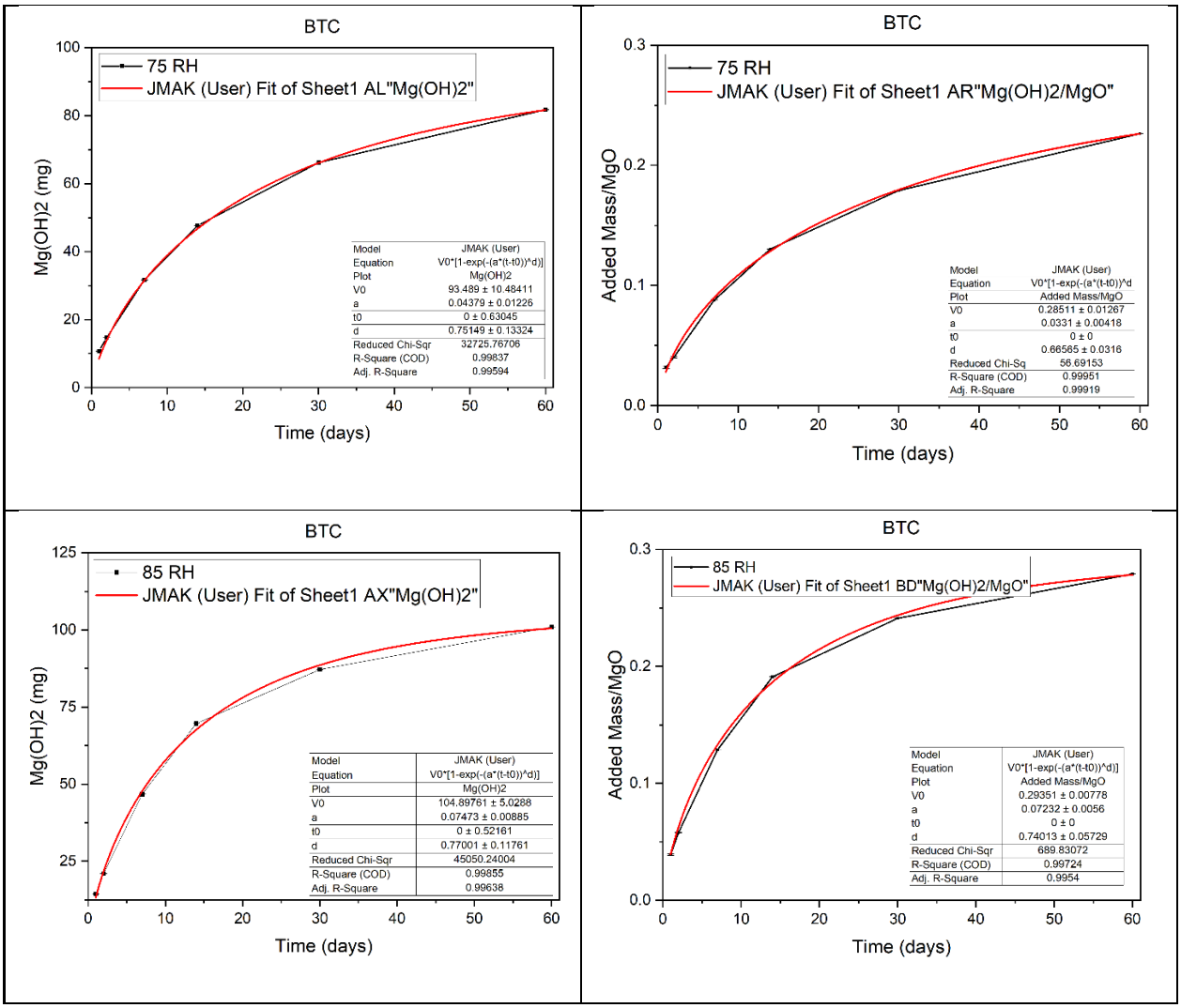

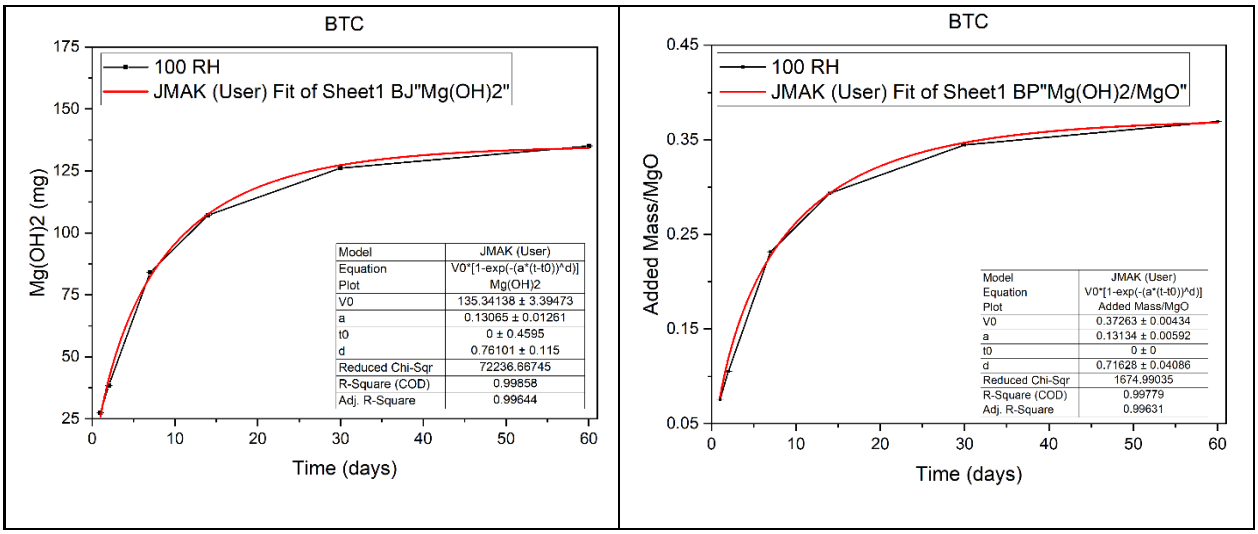

Figure 34: : Data fitting for the BTC powder at 75%, 85% and 100 % RH.

4.2.1.3 Sky Springs (SS)

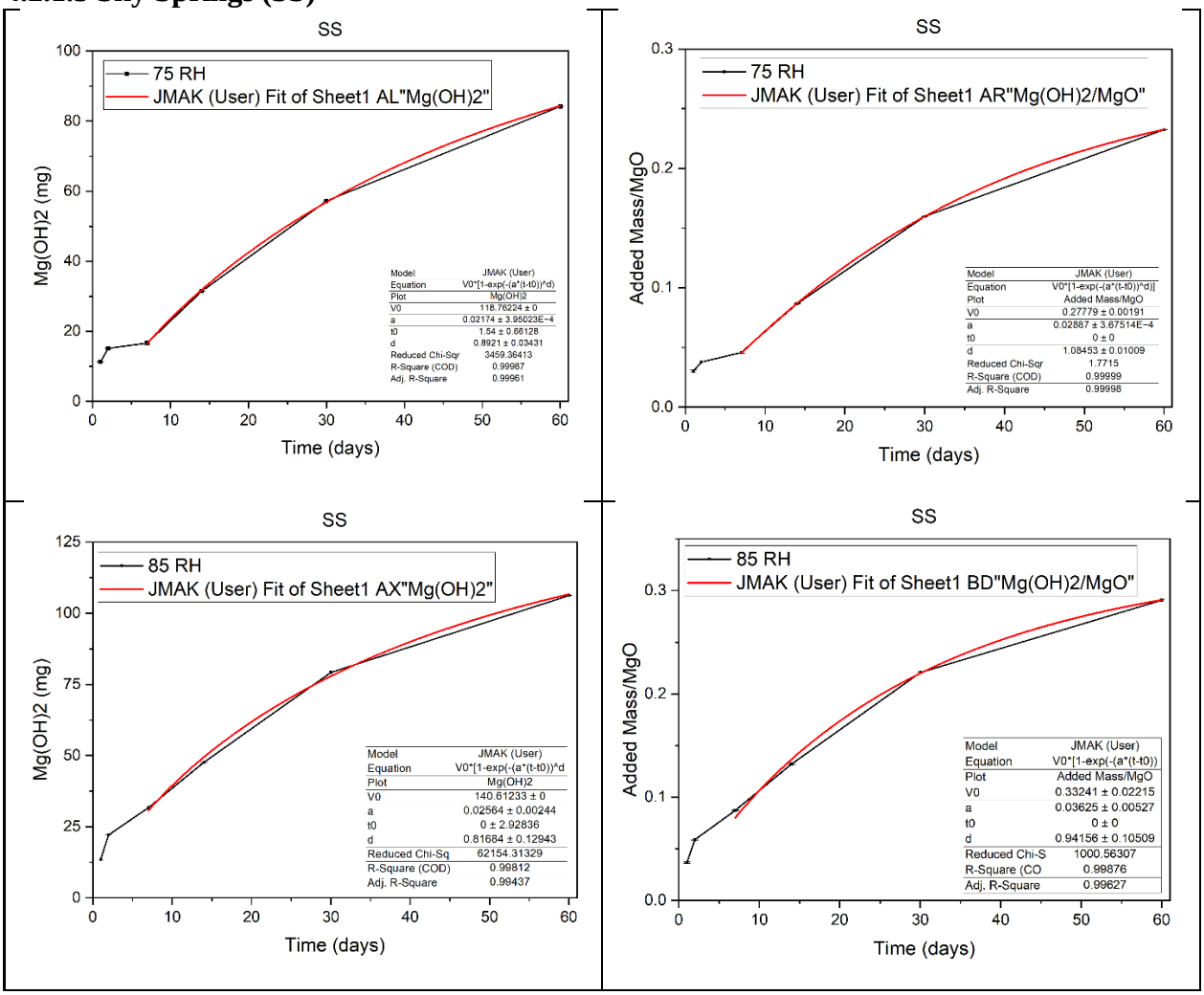

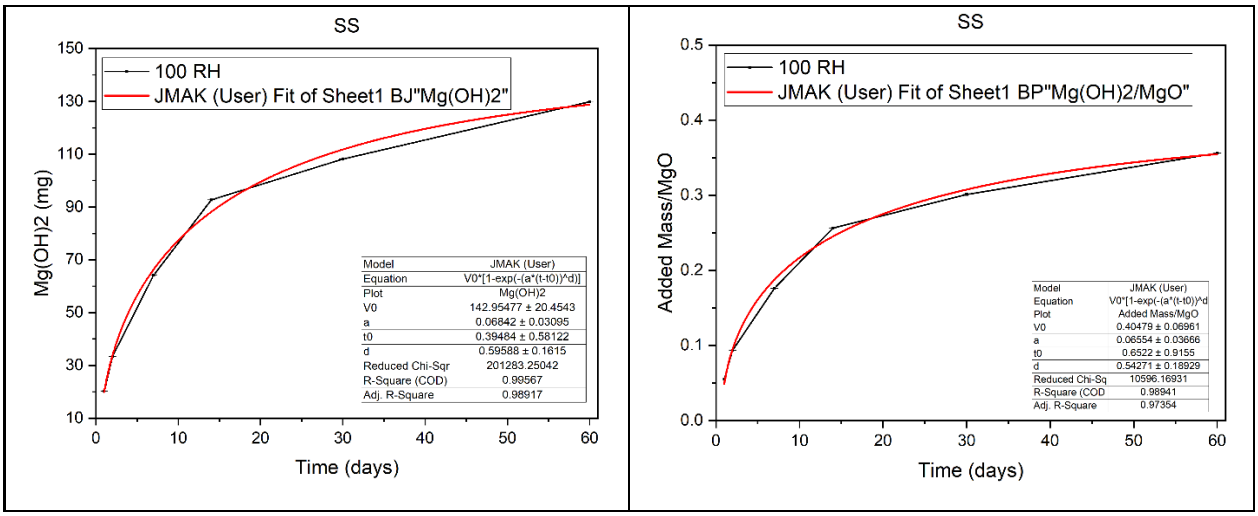

Figure 35: : Data fitting for the SS powder at 75%, 85% and 100 % RH.

Information containing the values of all parameters is displayed in the following table.

Table 4: Parameters of the experiments at 75%, 85% and 100% RH.

Powder	RH	M_0 (mg)	a (1/days)	t_0(days)	d
AA	**75 RH**	89.70215 ± 1.02787E-14	0.03777 ± 1.40845E-17	2.23328E-12 ± 9.42896E-15	3.5921 ± 2.42452E-15
AA	**85 RH**	101.84761 ± 7.49687	0.04378 ± 0.05728	0 ± 27.52861	3.18059 ± 4.55143
AA	**100 RH**	148.38829 ± 9.22848	0.04518 ± 0.00763	0 ± 2.99208	1.49687 ± 0.43188
BTC	**75 RH**	93.489 ± 10.48411	0.04379 ± 0.01226	0 ± 0.63045	0.75149 ± 0.13324
BTC	**85 RH**	104.89761 ± 5.0288	0.07473 ± 0.00885	0 ± 0.52161	0.77001 ± 0.11761
BTC	**100 RH**	135.34138 ± 3.39473	0.13065 ± 0.01261	0 ± 0.4595	0.76101 ± 0.115
SS	**75 RH**	118.76224 ± 0	0.02174 ± 3.95023E-4	1.54 ± 0.66128	0.8921 ± 0.03431
SS	**85 RH**	140.61233 ± 0	0.02564 ± 0.00244	0 ± 2.92836	0.81684 ± 0.12943
SS	**100 RH**	142.95477 ± 20.4543	0.06842 ± 0.03095	0.39484 ± 0.58122	0.59588 ± 0.1615

Data fitting using SasView was performed on the plots obtained for the SAXS and WAXS experiments. These fittings were carried out in two different regions, one per kind of experiment. The region for the SAXS fitting was in the range from Q= 0.00483288 1/Å to Q= 0.3 1/Å. For the WAXS the fitting was performed in the regions where the peaks appeared, this range was from Q=0.78 1/Å to Q=1.78 1/Å. For the SAXS fitting, the model used is given by [28]:

$$I(Q) = background + \sum_{i=1}^{2}\left[G_i \exp\left(-\frac{Q^2 R_{gi}^2}{3}\right) + B_i \exp\left(-\frac{Q^2 R_{g(i+1)}^2}{3}\right)\left(-\frac{1}{Q_i^2}\right)^{P_i}\right] \quad (24)$$

Where:

$$Q_i^2 = Q\left[\mathrm{erf}\left(\frac{QR_{gi}}{\sqrt{6}}\right)\right]^{-3} \quad (25)$$

In this model, G_i and B_i are constants [cm^{-1}], R_g is the radius of gyration [Å], and P_i is a power.

For the WAXS fitting, the model used is a linear combination of two Lorentzian peaks. The model is given by:

$$I(Q) = \sum_{i=1}^{2} \frac{A_i}{\left(1 + \left(\frac{Q - Q_{0i}}{B}\right)\right)} + background \quad (26)$$

Where A_i is the scale factor of the peak, Q_{0i} [1/Å] is the center of the peak having a half-width half-maximum (HWHM) of B [1/Å].

5. Discussion

5.1 QCM-D

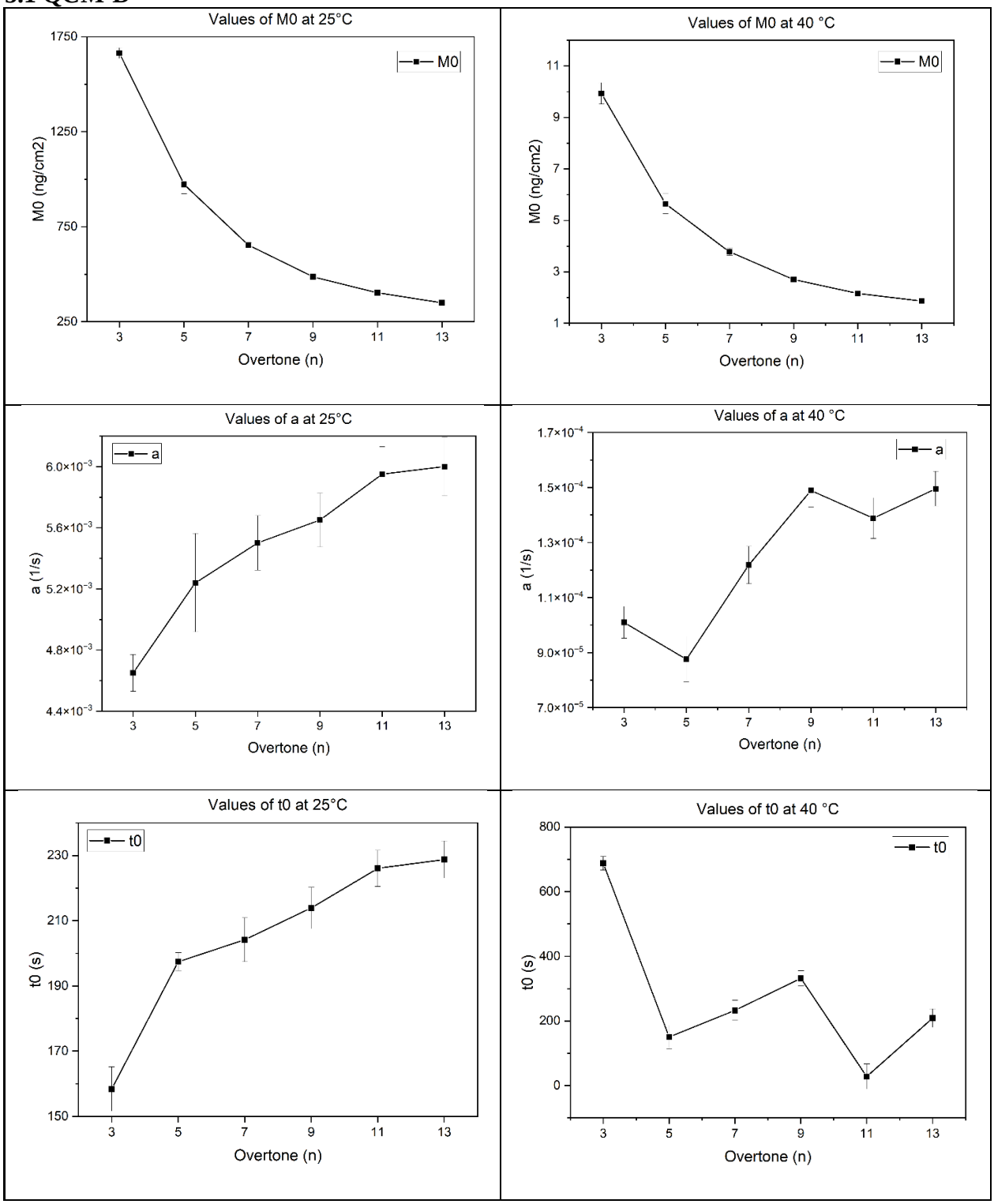

Figure 36: From top to the bottom: Plots of the values of the constants a, M_0 and t_0 for the QCM-D experiments at 25 C (left) and 40 C (right).

In the QCM-D experiments, as the overtone increases, the growth rate for $Mg(OH)_2$ decreases for both temperatures at which the experiments were conducted. This result becomes more evident when analyzing the plots for the values of M_0, where it is observed that the decrease in M_0 values for both experiments follows a similar trend.

The values of the rate constant (α) increased with the overtone in the experiment at 25 °C. However, in the experiment at 40 °C, there were two notable decreases in the value of this parameter: at overtones n=5 and n=11 .

Regarding the values of t_0, the two experiments exhibited divergent behaviors in the change of this parameter as a function of the overtones. In the experiment at 25 °C, the value of t_0 increased with the overtone; whereas in the experiment at 40 °C, the value decreased from n=3 to n=5 , then an increase was observed at n=7 and n=9 , followed by a third decrease at n=11 , and finally, an increase was observed at n=13.

5.2 Changes of mass of the powders

The values of the different parameters of equation (23) were plotted for all powders in figure 37.

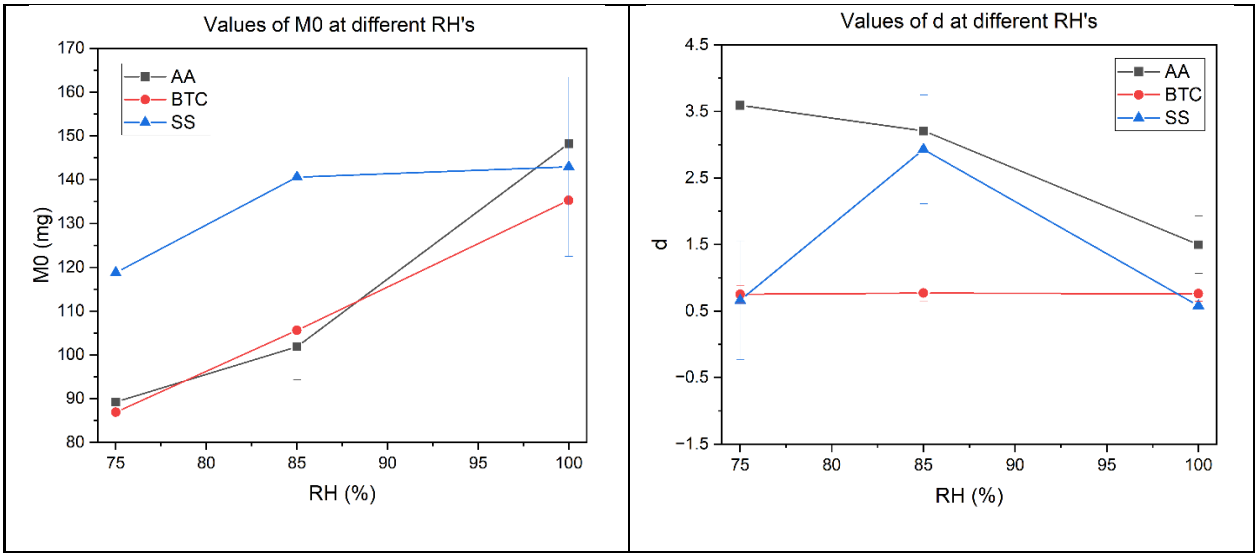

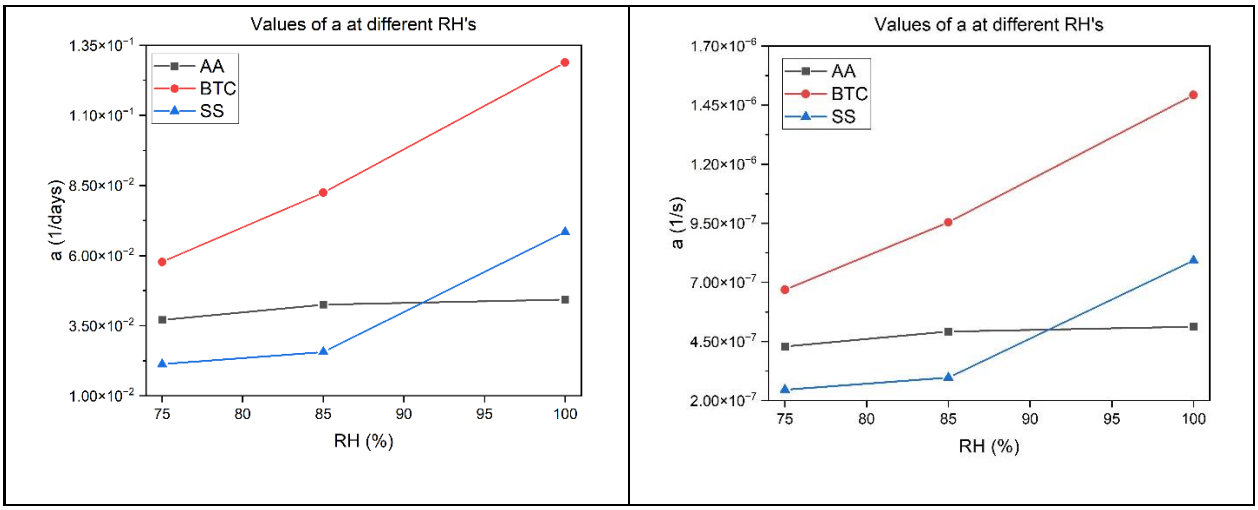

Figure 37: Plots of the values of the constants M0, α and d for the batch experiments.

The values of M_0 for the changes in mass of the powders exhibit an overall increase as a function of relative humidity.

Regarding dimensionality (d), each powder displays unique behavior: the AA powder's dimensionality demonstrates a decreasing trend; the BTC powder shows no significant change in this parameter; and the SS powder's d values increased from 75% RH to 85% RH, then decreased from 85% RH to 100% RH, with d at 75% RH and 100% RH having comparable values.

The rate constant (a) shows an increasing trend for all powders, with the BTC powder possessing the highest values at all RH levels. This parameter was greater for the AA powder than for the SS powder at 75% RH and 85% RH. However, at 100% RH, this trend reversed, with the SS powder exhibiting a higher rate constant than the AA powder.

5.3 SAXS/WAXS

The values of the different parameters of equation (24) and are plotted in figures 38, 39 and 40 for all powders.

5.3.1 SAXS

5.3.1.1 AA

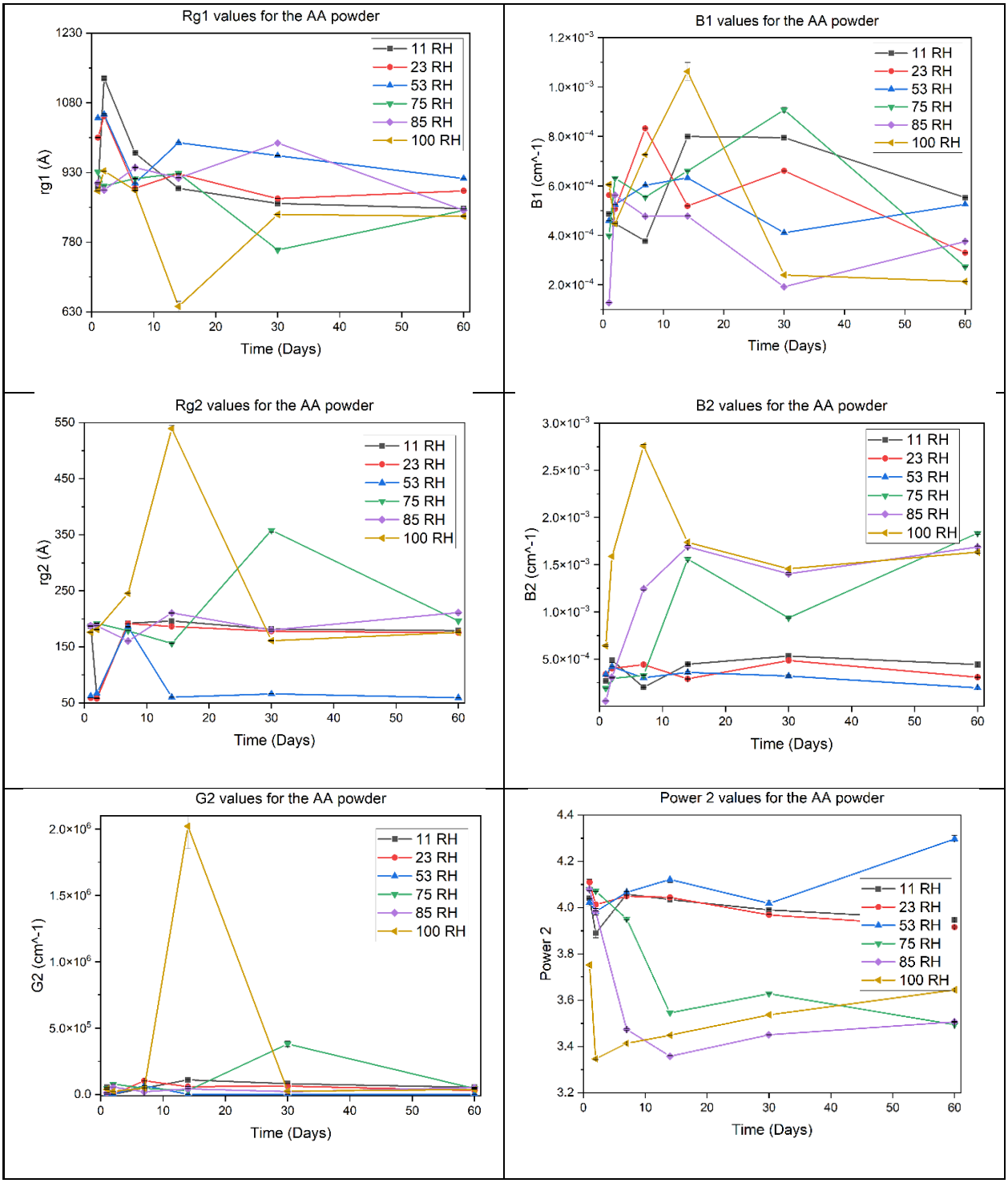

Figure 38: Values of the different parameters obtained for the fitting of the AA powder.

The radius of gyration at the first level (Rg1) displayed a decreasing trend as a function of exposure time across all relative humidity (RH) levels. In contrast, the radius of gyration at the second level (Rg2) showed an increasing trend for all exposure times at all RH levels, with the exception of the one at 53% which showed an increase after an exposure time of 1 week after this time, its value decreased and kept comparable values in comparison with its original one.

The scale factor for the power-law term (B1) at the first level also decreased as a function of exposure time for all RH levels. Conversely, the scale factor for the power-law term at the second level (B2) exhibited an increasing trend for all exposure times across all RH levels, with the highest three RH levels having noticeably larger values than those at the lowest RH levels.

The exponent of the power-law term at the second level (Power 2) showed a decreasing trend for all exposure times across all RH levels, with the highest three RH levels having visibly smaller values than those at the lowest RH levels.

The scale factor associated with the Guinier term (G2) at the second level demonstrated a consistent decline for the 11% and 53% RH levels up to a two-week exposure period. Following this duration, the G2 values for these specific RH conditions continued to show a downward trajectory. Conversely, the other RH levels generally followed a declining pattern in their respective G2 values, with notable exceptions being slight increases observed at the 75%, 85%, and 100% RH levels after one month of exposure. The latter also exhibited an increase after 2-weeks exposure eventually decreasing its value after this time.

5.3.1.2 BTC

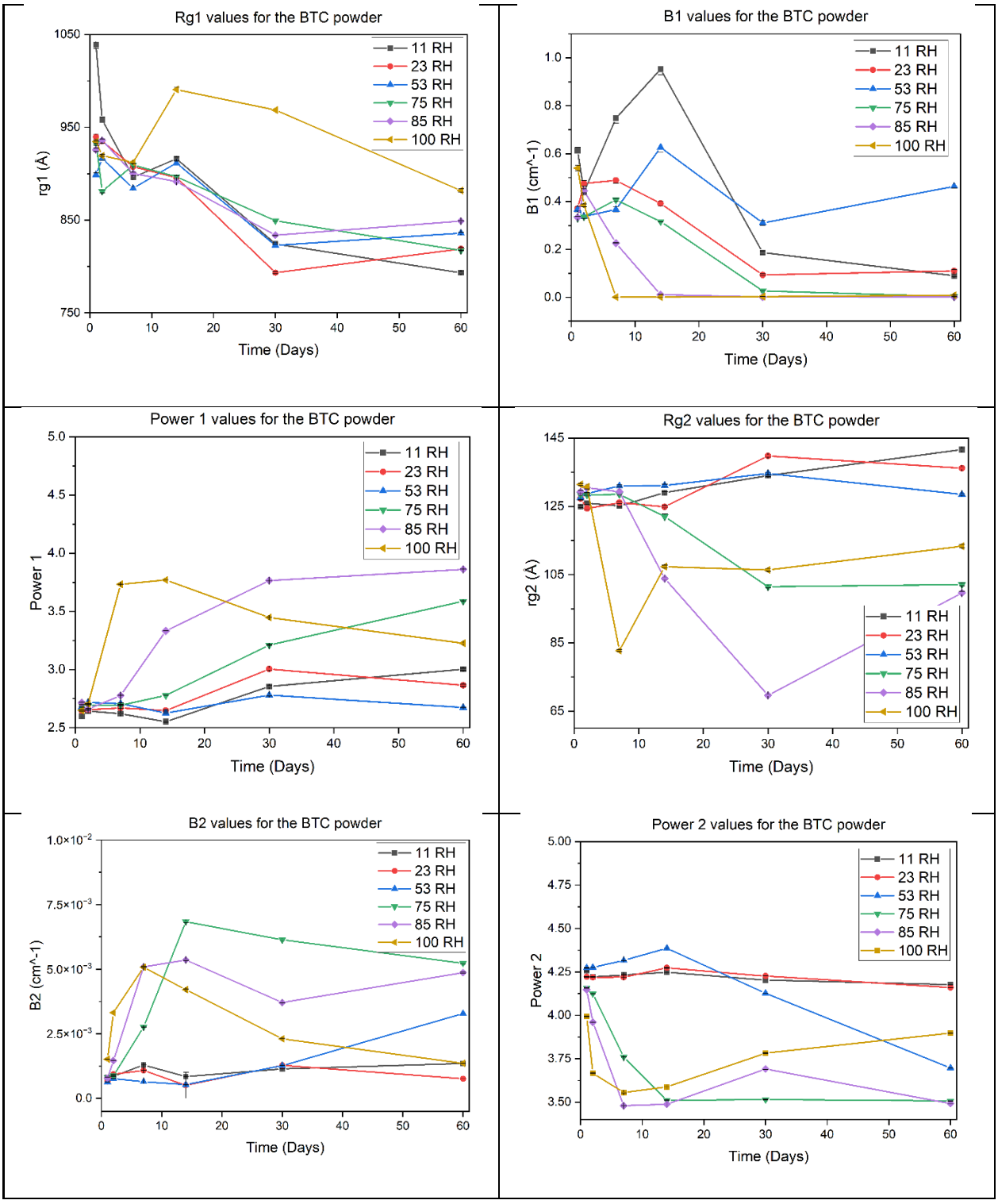
Rg1 values for the BTC powder
rg1 (Å)
Time (Days)
B1 values for the BTC powder
B1 (cm^-1)
Time (Days)
Power 1 values for the BTC powder
Power 1
Time (Days)
Rg2 values for the BTC powder
rg2 (Å)
Time (Days)
B2 values for the BTC powder
B2 (cm^-1)
Time (Days)
Power 2 values for the BTC powder
Power 2
Time (Days)
11 RH
23 RH
53 RH
75 RH
85 RH
100 RH

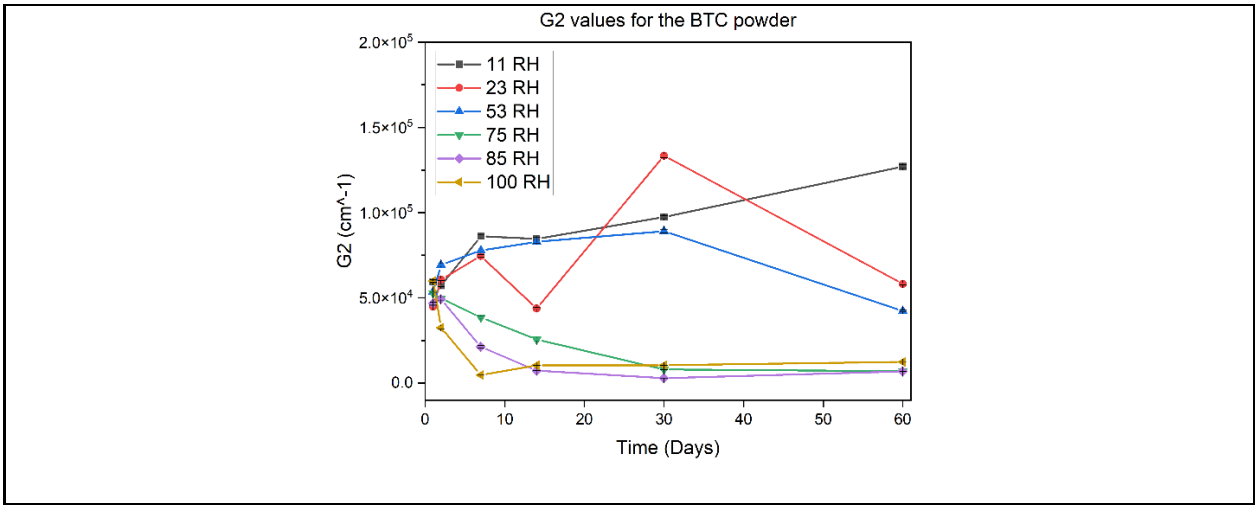

Figure 39: Values of the different parameters obtained for the fitting of the BTC powder.

The radius of gyration at the first level (Rg1) exhibited a decreasing trend as a function of exposure time across all relative humidity (RH) levels, with the lowest RH levels showing higher values after a 2-month exposure period. Similarly, the radius of gyration at the second level (Rg2) demonstrated a decreasing trend for all exposure durations at all RH levels, with the highest three RH levels having significantly larger values than those at the lowest RH levels.

The scale factor for the power-law term (B1) at the first level decreased with exposure time for all RH levels. In contrast, the scale factor for the power-law term at the second level (B2) showed an increasing trend up to a 2-week exposure across all RH levels, with the highest three RH levels displaying notably larger values than those at the lowest RH levels. Beyond this exposure duration, the values for the three aforementioned RH levels began to decrease.

The exponent of the power-law term at the first level (Power 1) indicated an increasing trend as a function of exposure time for three RH levels, with the exceptions being at 23% RH, 53% RH, and 100% RH, which exhibited a decreasing trend after a 1-month exposure. Conversely, the exponent of the power-law term at the second level (Power 2) decreased for all exposure durations across

all RH levels, with the highest three RH levels showing significantly smaller values than those at the lowest RH levels.

The scale factor for the Guinier term (G2) at the second level displayed a decreasing trend for all exposure durations, except at 11% RH, where the highest three RH levels had noticeably smaller values than those at the lowest RH levels.

5.3.1.3 SS

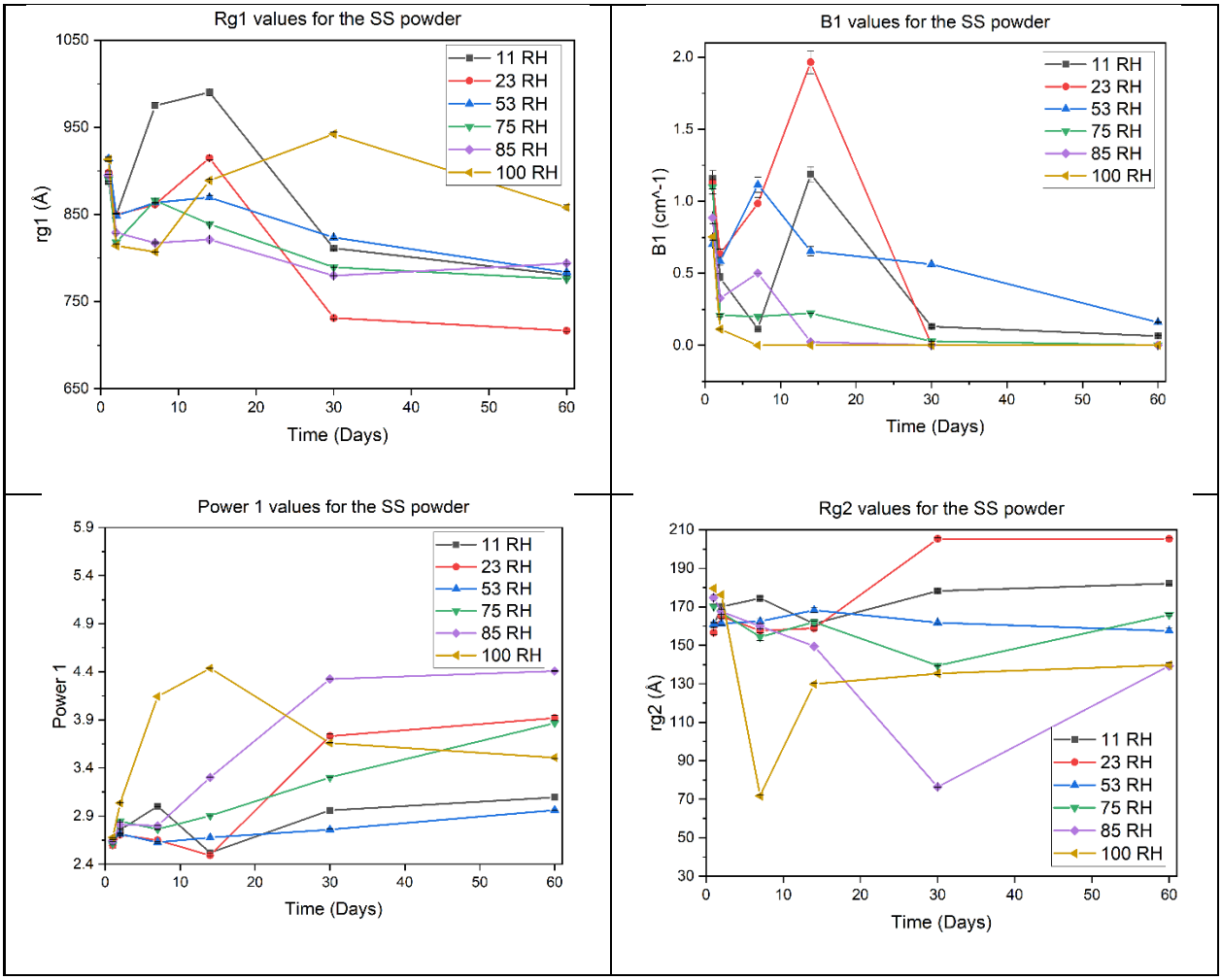

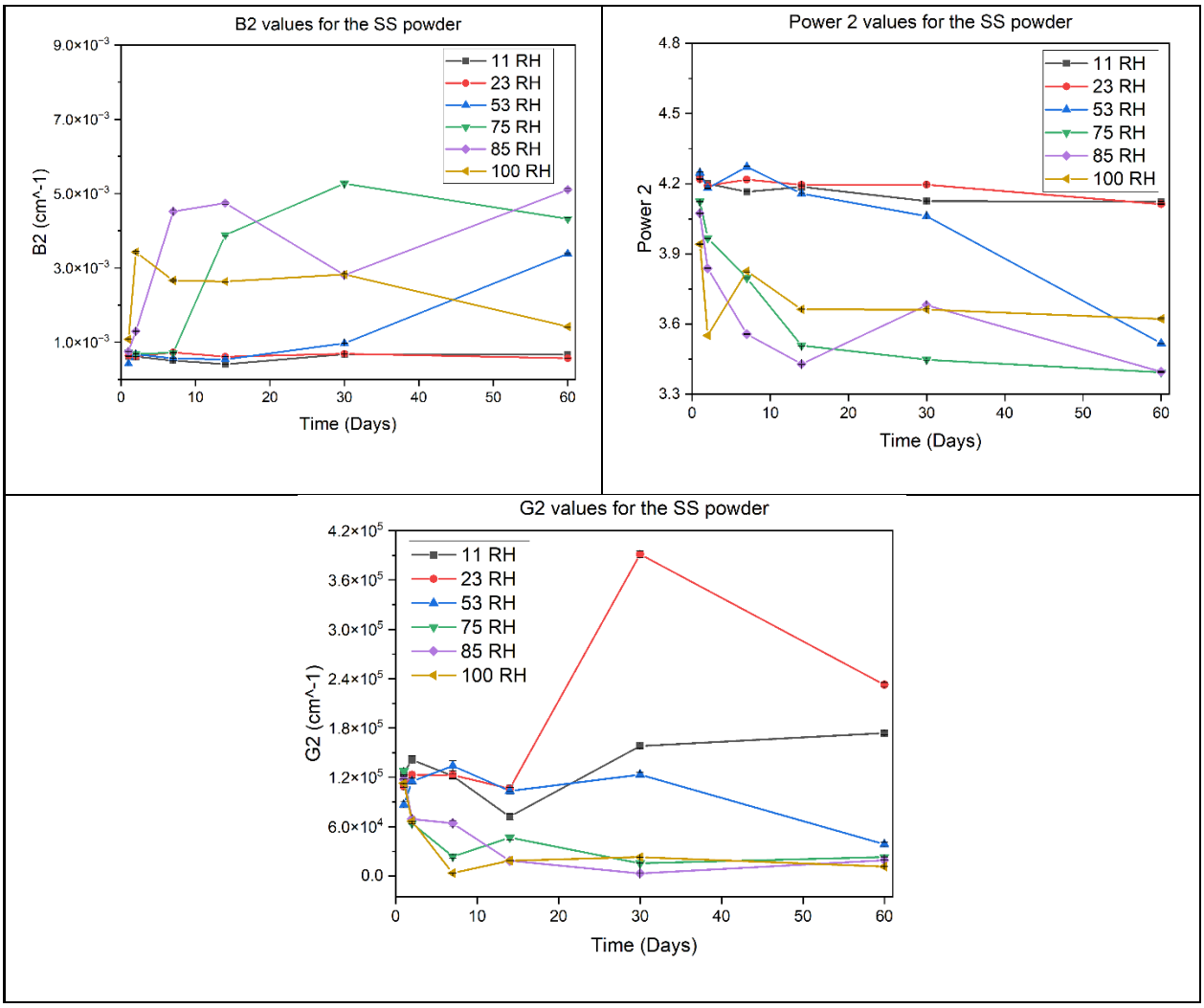

Figure 40: Values of the different parameters obtained for the fitting of the SS powder.

The radius of gyration at the first level (Rg1) exhibited a decreasing trend as a function of exposure time across all relative humidity (RH) levels, with the lowest RH levels showing higher values after a 2-month exposure period. Similarly, the radius of gyration at the second level (Rg2) demonstrated a decreasing trend for all exposure durations at all RH levels, except at 11% RH and 23% RH.

The scale factor for the power-law term (B1) at the first level decreased with exposure time for all RH levels. In contrast, the scale factor for the power-law term at the second level (B2) showed an increasing trend up to a 1-month exposure across all RH levels, with the highest three RH levels

displaying notably larger values than those at the lowest RH levels. Beyond this exposure duration, the values for two of the three aforementioned RH levels began to decrease, the exception being the one for the 75% RH.

The exponent of the power-law term at the first level (Power 1) indicated an increasing trend as a function of exposure time for all RH levels, with the exception being at 100% RH, which exhibited a decreasing trend after a 2-week exposure. Conversely, the exponent of the power-law term at the second level (Power 2) decreased for all exposure durations across all RH levels, with the highest three RH levels showing significantly smaller values than those at the lowest RH levels.

The scale factor for the Guinier term (G2) at the second level displayed a decreasing trend for all exposure durations, except at 11% RH and 23% RH, where the highest three RH levels had noticeably smaller values than those at the lowest RH levels.

5.3.2 WAXS

The values of the different parameters of equation (26) are plotted in figures 41, 42 and 43 for all powders.

5.3.2.1 AA

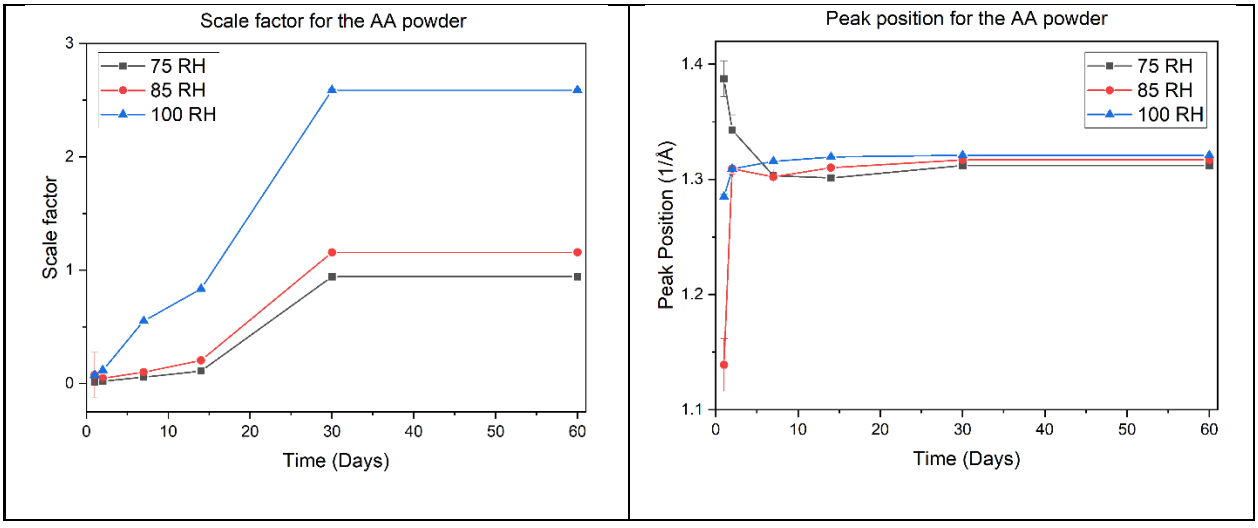

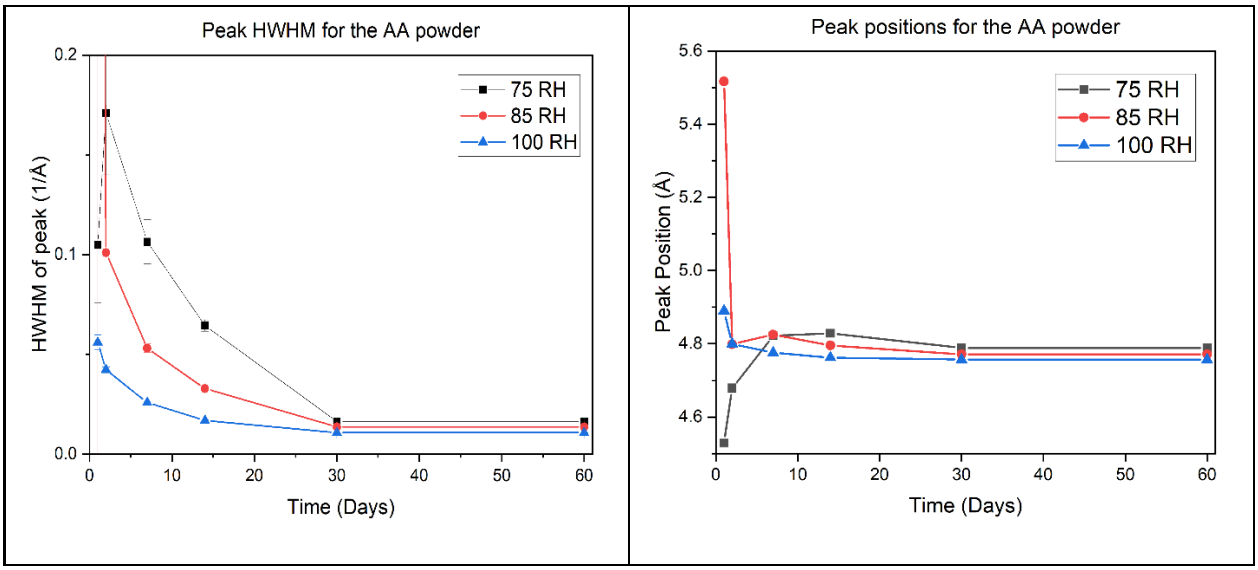

Figure 41: Values of the different parameters obtained for the fitting of the AA powder.

The scale factor demonstrated a consistent increasing trend as a function of exposure time across all relative humidity (RH) levels. The peak positions of the highest peak remained comparable across all RH levels, with the values converging approximately at 1.3 1/Å. Similarly, the half-width at half-maximum (HWHM) values of the peaks were also consistent across all RH levels, averaging around 0.01 1/Å.

5.3.2.2 BTC

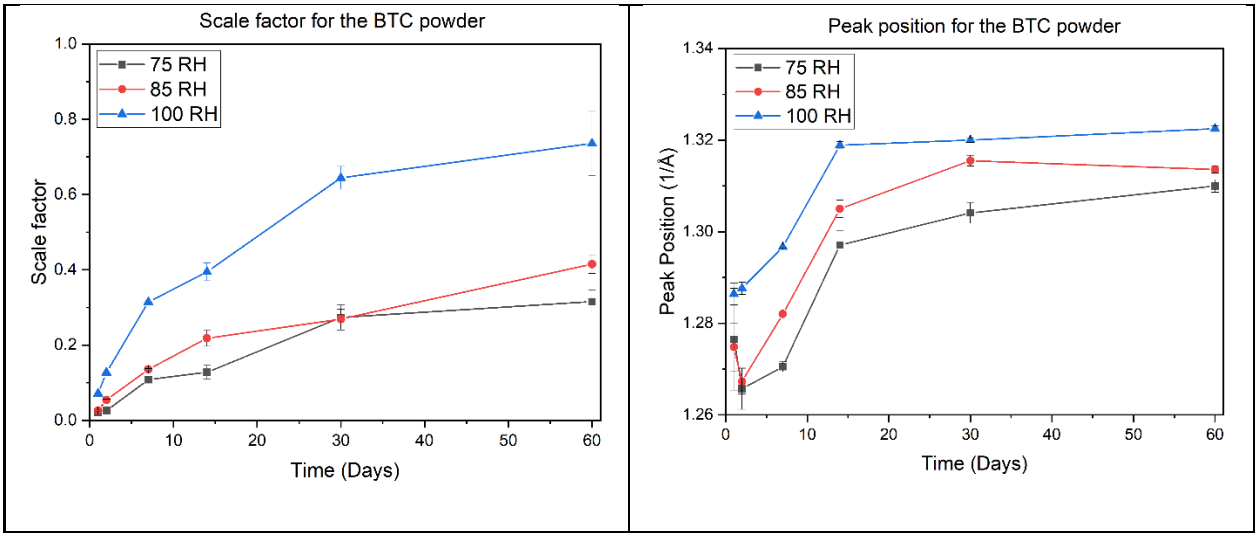

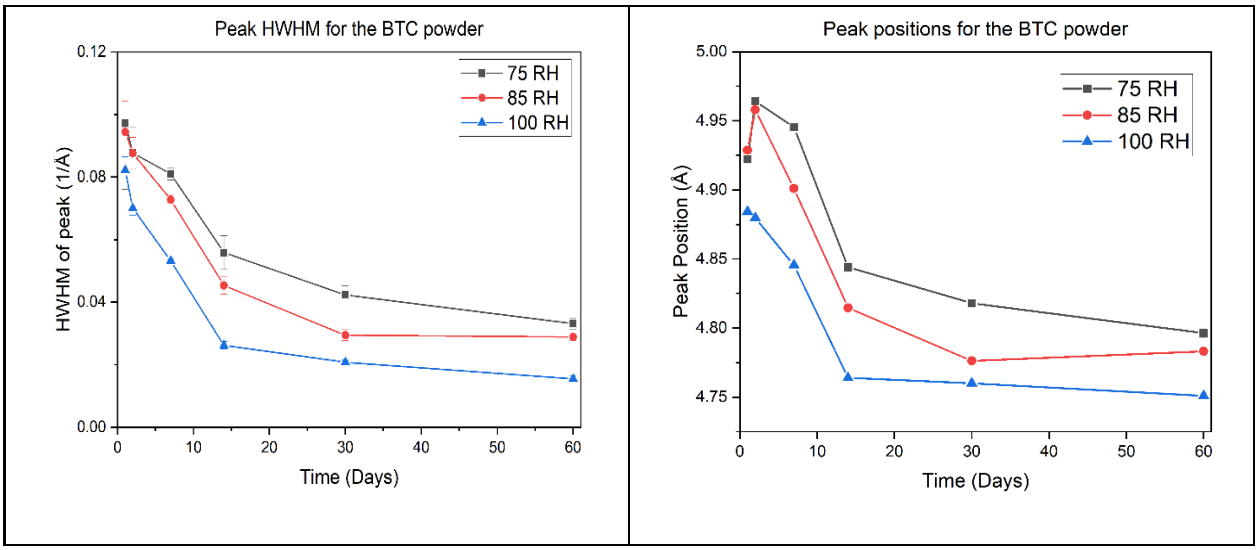

Figure 42: Values of the different parameters obtained for the fitting of the BTC powder.

The scale factor demonstrated a consistent increasing trend as a function of exposure time across all relative humidity (RH) levels, with the scale factor having comparable values for the 75% RH and 85% RH at 1-month exposure time. The peak positions of the highest peak remained comparable across all RH levels, with the values converging approximately at 1.31 1/Å. Similarly, the half-width at half-maximum (HWHM) values of the peaks consistently decreased for all exposure durations across all RH levels, converging around 0.01 1/Å.

5.3.2.3 SS

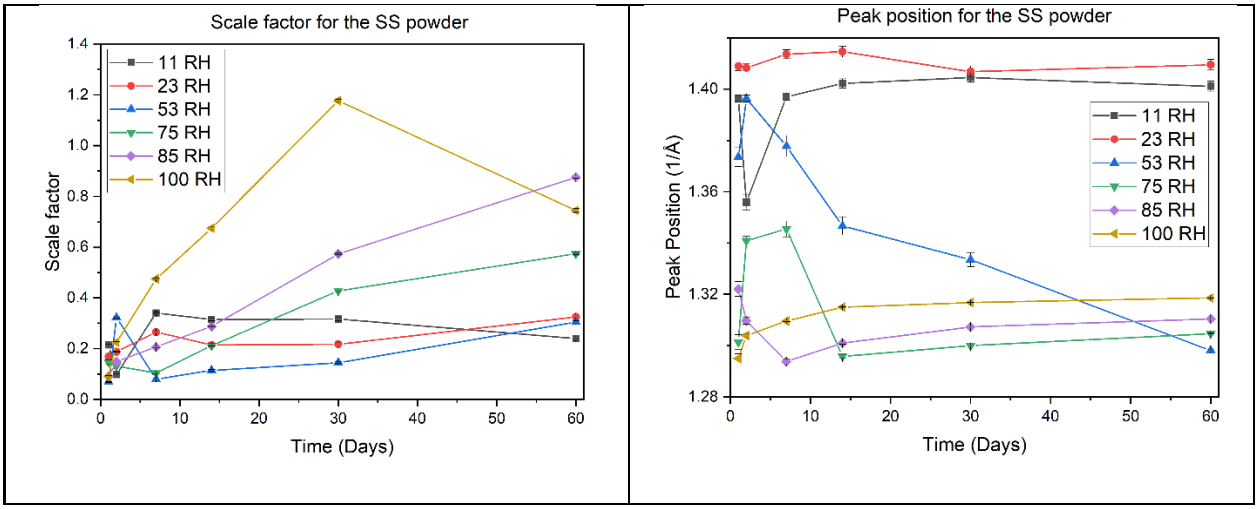

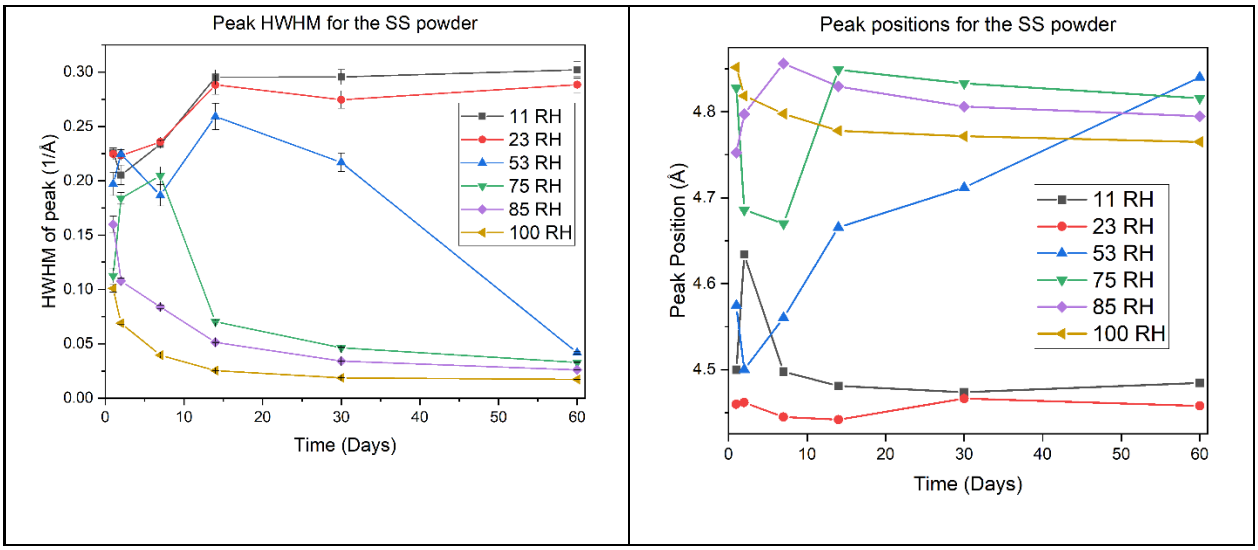

Figure 43: Values of the different parameters obtained for the fitting of the SS powder.

The scale factor exhibited a consistent increasing trend as a function of exposure time across all relative humidity (RH) levels, with the exception of 11% RH and 100% RH, which showed a decreasing trend after one month.

The peak positions of the highest peak varied: at the two lowest RH levels, they increased, converging around 1.4 1/Å. For 53% RH, the peak positions initially increased, mirroring the trend of the lower RH levels until a 2-day exposure, then decreased, stabilizing around 1.30 1/Å. The highest three RH levels saw a consistent decrease, resulting in values significantly smaller than those at the lower RH levels, converging around 1.3 1/Å.

The half-width at half-maximum (HWHM) values of the peaks also diverged: those at the two lowest RH levels increased, converging around 0.29 1/Å. For 53% RH, the HWHM values increased following the same initial trend until a 1-month exposure, after which they decreased, converging around 0.03 1/Å. The highest three RH levels consistently decreased, with values significantly smaller than those at the lower RH levels, converging around 0.03 1/Å.

With the values of M_0 obtained in the previous data analysis, the rate constants (a), and the surface area of each powder, the brucite growth rates were obtained. The plots for these values are displayed in the following figures and their numerical values are displayed in the following tables.

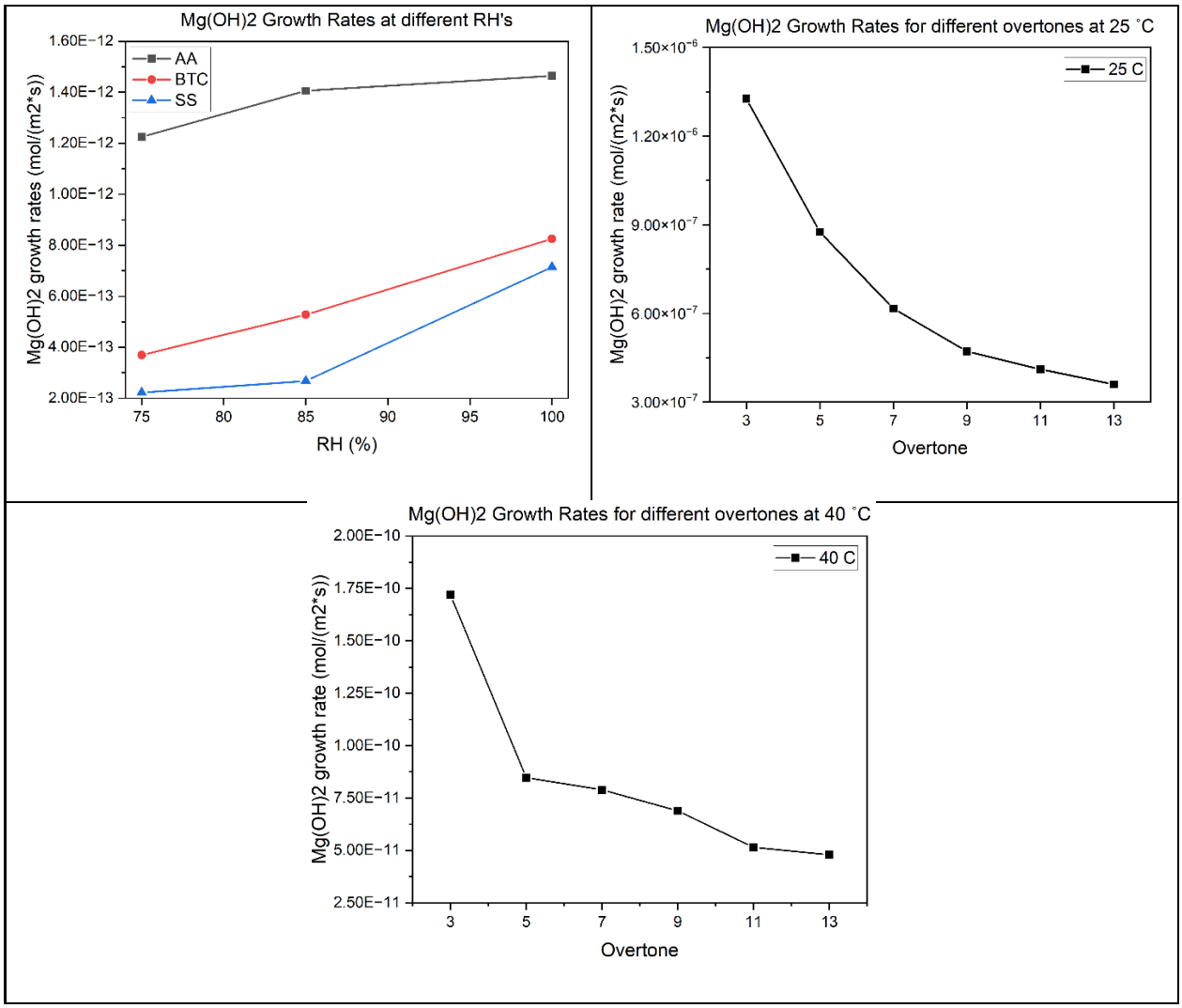

Figure 44: Mg(OH)2 growth rates obtained during the experiments.

The values presented in the previous figures are shown in the tables below.

Table 4: $Mg(OH)_2$ growth rates obtained from the batch experiments.

	AA	**BTC**	**SS**
75 RH	1.22515E-12 mol/(m^2*s)	3.6971E-13 mol/(m^2*s)	2.22274E-13 mol/(m^2*s)

85 RH	1.40575E-12 mol/(m^2*s)	5.27645E-13 mol/(m^2*s)	2.67815E-13 mol/(m^2*s)
100 RH	1.46463E-12 mol/(m^2*s)	8.25142E-13 mol/(m^2*s)	7.14662E-13 mol/(m^2*s)

Table 5: $Mg(OH)_2$ growth rates obtained from the QCM experiments.

Overtone (n)	**25 ˚C**	**40 ˚C**
3	1.3266E-6 mol/(m^2*s)	1.7199E-10 mol/(m^2*s)
5	8.75381E-7 mol/(m^2*s)	8.4742E-11 mol/(m^2*s)
7	6.16202E-7 mol/(m^2*s)	7.89107E-11 mol/(m^2*s)
9	4.71418E-7 mol/(m^2*s)	6.89292E-11 mol/(m^2*s)
11	4.11065E-7 mol/(m^2*s)	5.14644E-11 mol/(m^2*s)
13	3.59748E-7 mol/(m^2*s)	4.79043E-11 mol/(m^2*s)

6. Conclusions

The growth rates observed in this thesis were found to be dependent on the experimental conditions and the type of experiment conducted.

Specifically, the QCM analysis, which was performed with water flowing at a constant rate and fixed temperature, revealed brucite growth rates spanning two orders of magnitude. The experiment conducted at 25°C yielded growth rates, ranging from 10^{-7}-10^{-6} mol/(m^2s) over a range between 180 seconds to 570 seconds after the experiment began.

Conversely, the experiment at 40°C exhibited markedly different kinetics, with growth rates between 10^{-11} - 10^{-10} mol/(m^2s). This variation was recorded over an extended duration, commencing at the onset of the experiment, and persisting up to 8000 seconds.

In the batch experiments, where powders with varying surface areas were subjected to different relative humidity (RH) levels over various exposure times, distinct growth rates were observed for each powder. The AA powder demonstrated rates on the order of 10^{-12} mol/(m^2s). The BTC and SS powders exhibited growth rates on the order of 10^{-13} mol/(m^2s), with the SS powder showing the smallest values among the three.

WAXS data from the batch experiments indicated brucite growth at the three highest RH levels: 75%, 85%, and 100% for both AA and BTC powders. The intensity values increased with RH level, and the peak intensities also rose as a function of exposure time. For the SS powder, rapid brucite growth was observed at the three lowest RH levels during the 1-day and 2-day experiments, with peak intensities surpassing those at higher RH levels. After one week of exposure, the intensity peaks for powders at the highest RH levels exceeded those at lower RH levels.

SAXS findings suggested a decrease in brucite particle size over time at the highest RH levels, implying an RH threshold beyond which brucite detaches from the magnesia. This detachment

reduces particle size and leaves unreacted magnesia surfaces available for further reaction with water, thereby promoting additional brucite growth.

It is important to note that these growth rates were obtained using different methods: in the QCM-D experiments, the growth rates were obtained in experiments in aqueous conditions . In the batch experiments, on the other hand, the growth rates were obtained through vapor exposition. Therefore these experiments, and their results, must be considered as complementary instead of equivalent ones.

7. References

[1] NOAA, "NOAA. ESRL Global Monitoring Division—Global Greenhouse Gas Reference Network." Accessed: Jan. 20, 2024. [Online]. Available: https://gml.noaa.gov/ccgg/trends/mlo.html

[2] Global Carbon Atlas, "CO2 emissions." Accessed: Jan. 22, 2024. [Online]. Available: https://globalcarbonatlas.org/emissions/carbon-emissions/

[3] J. G. Blencoe, D. A. Palmer, L. M. Anovitz, and J. S. Beard, "Carbonation of metal silicates for long-term CO2 sequestration," US 10,632,418 B2, Apr. 28, 2020

[4] K. S. Lackner, D. P. Butt, and C. H. Wendt, "Progress on binding CO2 in mineral substrates," *Energy Convers Manag*, vol. 38, no. SUPPL. 1, pp. S259–S264, Jan. 1997, doi: 10.1016/S0196-8904(96)00279-8.

[5] K. S. Lackner, C. H. Wendt, D. P. Butt, E. L. Joyce, and D. H. Sharp, "Carbon dioxide disposal in carbonate minerals," *Energy*, vol. 20, no. 11, pp. 1153–1170, Jan. 1995, doi: 10.1016/0360-5442(95)00071-N.

[6] N. McQueen, P. Kelemen, G. Dipple, P. Renforth, and J. Wilcox, "Ambient weathering of magnesium oxide for CO2 removal from air," *Nature Communications 2020 11:1*, vol. 11, no. 1, pp. 1–10, Jul. 2020, doi: 10.1038/s41467-020-16510-3.

[7] Y. Guo *et al.*, "Magnesium-based basic mixtures derived from earth-abundant natural minerals for CO2 capture in simulated flue gas," *Fuel*, vol. 243, pp. 298–305, May 2019, doi: 10.1016/J.FUEL.2019.01.108.

[8] K. Ho, S. Jin, M. Zhong, A. T. Vu, and C. H. Lee, "Sorption capacity and stability of mesoporous magnesium oxide in post-combustion CO2 capture," *Mater Chem Phys*, vol. 198, pp. 154–161, Sep. 2017, doi: 10.1016/J.MATCHEMPHYS.2017.06.002.

[9] K. K. Han, Y. Zhou, Y. Chun, and J. H. Zhu, "Efficient MgO-based mesoporous CO2 trapper and its performance at high temperature," *J Hazard Mater*, vol. 203–204, pp. 341–347, Feb. 2012, doi: 10.1016/J.JHAZMAT.2011.12.036.

[10] K. K. Han, Y. Zhou, W. G. Lin, and J. H. Zhu, "One-pot synthesis of foam-like magnesia and its performance in CO2 adsorption," *Microporous and Mesoporous Materials*, vol. 169, pp. 112–119, Mar. 2013, doi: 10.1016/J.MICROMESO.2012.11.004.

[11] R. C. Ropp, "Group 14 (C, Si, Ge, Sn, and Pb) Alkaline Earth Compounds," *Encyclopedia of the Alkaline Earth Compounds*, pp. 351–480, Jan. 2013, doi: 10.1016/B978-0-444-59550-8.00005-3.

[12] R. C. Ropp, "Group 16 (O, S, Se, Te) Alkaline Earth Compounds," in *Encyclopedia of the Alkaline Earth Compounds*, Elsevier, 2013, pp. 105–197. doi: 10.1016/B978-0-444-59550-8.00003-X.

[13] M. Edvardsson, "The working principles of QCM and QCM-D technology." Accessed: Jan. 24, 2024. [Online]. Available: https://www.biolinscientific.com/blog/how-does-qcm-technology-work

[14] M. Edvardsson, "The Sauerbrey equation. A brief explanation of what it is and how it is derived." Accessed: Jan. 24, 2024. [Online]. Available: https://www.biolinscientific.com/blog/what-is-the-sauerbrey-equation

[15] G. Sauerbrey, "Verwendung von Schwingquarzen zur Wägung dünner Schichten und zur Mikrowägung (Use of quartz crystals for weighing thin layers and micro-weighing)," *Zeitschrift für Physik*, vol. 155, no. 2, pp. 206–222, Apr. 1959, doi: 10.1007/BF01337937.

[16] M. Edvardsson, “Dissipation. What it is, why it is important, and how to measure it,” 2018. Accessed: Jan. 24, 2024. [Online]. Available: https://www.biolinscientific.com/blog/what-is-dissipation
[17] R.-J. Roe, *Methods of X-ray and Neutron Scattering in Polymer Science*. Oxford University Press, 2000.
[18] B. D. Cullity and S. R. Stock, *Elements of X-ray Diffraction*, 3rd ed. Addison-Wesley Publishing Company, 2013.
[19] “SAXS - What is Small And Wide Angle X-ray Scattering.” Accessed: Feb. 04, 2024. [Online]. Available: https://www.xenocs.com/knowledge-base/saxs/
[20] R. Pynn, *Los Alamos Science*, 1st ed. Los Alamos: Los Alamos National Laboratory, 1990.
[21] C. J. Gommes, S. Jaksch, and H. Frielinghaus, “Small-angle scattering for beginners,” *J Appl Crystallogr*, vol. 54, no. 6, pp. 1832–1843, Dec. 2021, doi: 10.1107/S1600576721010293.
[22] A. Guinier and G. Fournet, *Small Angle Scattering of X-rays.*, vol. 19. John Wiley & Sons, Inc. , 1955. doi: 10.1002/pol.1956.120199326.
[23] D. S. Sivia, *Elementary Scattering Theory*. Oxford University PressOxford, 2011. doi: 10.1093/acprof:oso/9780199228676.001.0001.
[24] L. A. Feigin and D. I. Svergun, *Structure Analysis by Small-Angle X-Ray and Neutron Scattering*. Boston, MA: Springer US, 1987. doi: 10.1007/978-1-4757-6624-0.
[25] “QSense Pro.” Accessed: Feb. 04, 2024. [Online]. Available: https://www.biolinscientific.com/qsense/instruments/qsense-pro
[26] L. Greenspan, “Humidity Fixed Points of Binary Saturated Aqueous Solutions,” *J Res Natl Bur Stand A Phys Chem*, vol. 81A, no. 1, p. 89, 1977, doi: 10.6028/JRES.081A.011.
[27] A. B. Brady *et al.*, “In Situ Observations of Barium Sulfate Nucleation in Nanopores,” *Cryst Growth Des*, vol. 22, no. 12, pp. 6941–6951, Dec. 2022, doi: 10.1021/acs.cgd.2c00592.
[28] G. Beaucage, “Small-Angle Scattering from Polymeric Mass Fractals of Arbitrary Mass-Fractal Dimension,” *J Appl Crystallogr*, vol. 29, no. 2, pp. 134–146, Apr. 1996, doi: 10.1107/S0021889895011605.

8. Appendix

The information contained in each column is explained as follows. All units are in micrograms.

- Column b: Mass of the empty vial.
- Column c: Mass of the empty vial and the sample added.
- Column d: Mass of the powder added.
- Column: e: Mass the vial and the powder added after RH exposure.
- Column f: Mass of the sample after RH exposure.
- Column g: Mass added after RH exposure.
- Column h: Mass of the vial and the sample after being heated in the oven at 120 ˚C for 24 hours.
- Column i: Mass of the sample after being heated in the oven at 120 ˚C for 24 hours.
- Column j: Mass of the water removed.
- Column k: Mass of the mineral added.

8.1 Alpha Aesar (AA)

Table 6: Values of the masses for the 1-day AA experiment.

AA	**1 day**									
A	**b**	**c**	**d=c-b**	**e**	**f=e-b**	**g**	**h**	**i=h-b**	**j**	**k**
11 RH	11006.1	11374.8	368.7	11374.9	368.8	0.1	11374.3	368.2	0.6	-0.5
23 RH	11015.3	11376.9	361.6	11377.4	362.1	0.5	11377.1	361.8	0.3	0.2
53 RH	10943.4	11311.7	368.3	11312.4	369	0.7	11313.3	369.9	-0.9	1.6
75 RH	10597.6	10967.1	369.5	10968.3	370.7	1.2	10969	371.4	-0.7	1.9
85 RH	10606.9	10969.2	362.3	10971.8	364.9	2.6	10970	363.1	1.8	0.8
100 RH	10547.6	10916.6	369	10926.4	378.8	9.8	10924.1	376.5	2.3	7.5

Table 7: Values of the masses for the 2-day AA experiment.

AA	2 days									
A	**b**	**c**	**d=c-b**	**e**	**f=e-b**	**g**	**h**	**i=h-b**	**j**	**k**
11 RH	10974	11344.8	370.8	11343	369	-1.8	11341.2	367.2	1.8	-3.6
23 RH	11061.9	11423.7	361.8	11424.6	362.7	0.9	11422.4	360.5	2.2	-1.3
53 RH	10912.6	11280.1	367.5	11281.7	369.1	1.6	11280.7	368.1	1	0.6
75 RH	10581.9	10942.4	360.5	10944.2	362.3	1.8	10942.8	360.9	1.4	0.4
85 RH	10654.3	11016.2	361.9	11021.3	367	5.1	11019.4	365.1	1.9	3.2
100 RH	10523	10887	364	10901.9	378.9	14.9	10898	375	3.9	11

Table 8: Values of the masses for the 1-week AA experiment.

AA	1 week									
A	**b**	**c**	**d=c-b**	**e**	**f=e-b**	**g**	**h**	**i=h-b**	**j**	**k**
11 RH	10604	10965.1	361.1	10966.78	362.78	1.68	10966.09	362.09	0.69	0.99
23 RH	11060.3	11426.3	366	11429.72	369.42	3.42	11428.61	368.31	1.11	2.31
53 RH	10580.8	10948.6	367.8	10953.28	372.48	4.68	10952.61	371.81	0.67	4.01
75 RH	10630.51	10992.81	362.3	10998.34	367.83	5.53	10997.75	367.24	0.59	4.94
85 RH	10693.1	11055.8	362.7	11068.61	375.51	12.81	11067.86	374.76	0.75	12.06
100 RH	10650.9	11015.1	364.2	11045.75	394.85	30.65	11039.64	388.74	6.11	24.54

Table 9: Values of the masses for the 2-week AA experiment.

AA	2 weeks									
A	**b**	**c**	**d=c-b**	**e**	**f=e-b**	**g**	**h**	**i=h-b**	**j**	**k**
11 RH	10990	11357.8	367.8	11362.79	372.79	4.99	11358.38	368.38	4.41	0.58
23 RH	11611.2	11977.4	366.2	11984.02	372.82	6.62	11980.52	369.32	3.5	3.12
53 RH	10564.7	10926.9	362.2	10935.18	370.48	8.28	10933.73	369.03	1.45	6.83
75 RH	10551.2	10916.4	365.2	10928.53	377.33	12.13	10924.33	373.13	4.2	7.93
85 RH	10504	10869.2	365.2	10889.7	385.7	20.5	10886.08	382.08	3.62	16.88
100 RH	10611.3	10979.3	368	11045.34	434.04	66.04	11035.01	423.71	10.33	55.71

Table 10: Values of the masses for the 1-month AA experiment.

AA	1 month									
A	b	c	d=c-b	e	f=e-b	g	h	i=h-b	j	k
11 RH	10638.9	10997	358.1	11003.97	365.07	6.97	11003.58	364.68	0.39	6.58
23 RH	10915.8	11275	359.2	11285.32	369.52	10.32	11286.07	370.27	-0.75	11.07
53 RH	10679.7	11037.9	358.2	11051.29	371.59	13.39	11053.25	373.55	-1.96	15.35
75 RH	10564.4	10924.7	360.3	10996.53	432.13	71.83	10995.78	431.38	0.75	71.08
85 RH	10582.1	10943	360.9	11043.37	461.27	100.37	11036.35	454.25	7.02	93.35
100 RH	10640.3	10997.8	357.5	11142.23	501.93	144.43	11117.94	477.64	24.29	120.14

Table 11:Values of the masses for the 2-month AA experiment.

AA	2 months									
A	b	c	d=c-b	e	f=e-b	g	h	i=h-b	j	k
11 RH	10641.1	11000.2	359.1	11014.83	373.73	14.63	11014.3	373.2	0.53	14.1
23 RH	10575	10937	362	10970.69	395.69	33.69	10967.64	392.64	3.05	30.64
53 RH	10500.8	10865.3	364.5	10929.48	428.68	64.18	10924.71	423.91	4.77	59.41
75 RH	10663.1	11026.1	363	11123.69	460.59	97.59	11115.76	452.66	7.93	89.66
85 RH	10587.2	10949.1	361.9	11058.89	471.69	109.79	11050.35	463.15	8.54	101.25
100 RH	10640	11008.3	368.3	11208.89	568.89	200.59	11154.1	514.1	54.79	145.8

8.2 Beantown Chemical (BTC)

Table 12: Values of the masses for the 1-day BTC experiment.

BTC	1 day									
A	b	c	d=c-b	e	f=e-b	g	h	i=h-b	j	k
11 RH	10544.6	10931.1	386.5	10933.2	388.6	2.1	10930.8	386.2	2.4	-0.3
23 RH	10989.4	11382.4	393	11383.9	394.5	1.5	11380.4	391	3.5	-2

53 RH	11344.5	11725.5	381	11732.7	388.2	7.2	11727.9	383.4	4.8	2.4
75 RH	11386.8	11724.8	338	11738.9	352.1	14.1	11735.5	348.7	3.4	10.7
85 RH	10602.2	10971.6	369.4	10991.5	389.3	19.9	10986	383.8	5.5	14.4
100 RH	11036.6	11402.2	365.6	11435	398.4	32.8	11429.7	393.1	5.3	27.5

Table 13: Values of the masses for the 2-day BTC experiment.

BTC	**2 days**									
A	**b**	**c**	**d=c-b**	**e**	**f=e-b**	**g**	**h**	**i=h-b**	**j**	**k**
11 RH	10908.2	11278.2	370	11281.4	373.2	3.2	11275.9	367.7	5.5	-2.3
23 RH	11149.7	11510.6	360.9	11512.1	362.4	1.5	11508.4	358.7	3.7	-2.2
53 RH	11432.2	11795.7	363.5	11802.4	370.2	6.7	11797.9	365.7	4.5	2.2
75 RH	10911.7	11278	366.3	11300.9	389.2	22.9	11292.7	381	8.2	14.7
85 RH	11342.3	11704.9	362.6	11737.8	395.5	32.9	11725.9	383.6	11.9	21
100 RH	10678.2	11042.3	364.1	11099.3	421.1	57	11080.7	402.5	18.6	38.4

Table 14: Values of the masses for the 1-week BTC experiment.

BTC	**1 week**									
A	**b**	**c**	**d=c-b**	**e**	**f=e-b**	**g**	**h**	**i=h-b**	**j**	**k**
11 RH	10869.8	11235.2	365.4	11238.12	368.32	2.92	11235.84	366.04	2.28	0.64
23 RH	11478.3	11844.5	366.2	11853.85	375.55	9.35	11848.3	370	5.55	3.8
53 RH	11416.4	11778	361.6	11789.06	372.66	11.06	11784.41	368.01	4.65	6.41
75 RH	10609.7	10971.05	361.35	11017.28	407.58	46.23	11002.74	393.04	14.54	31.69
85 RH	11403.9	11766.8	362.9	11837.18	433.28	70.38	11813.53	409.63	23.65	46.73
100 RH	11021.4	11384.2	362.8	11513.56	492.16	129.36	11468.22	446.82	45.34	84.02

Table 15: Values of the masses for the 2-week BTC experiment.

BTC	**2 weeks**									
A	**b**	**c**	**d=c-b**	**e**	**f=e-b**	**g**	**h**	**i=h-b**	**j**	**k**

11 RH	11315.9	11681.3	365.4	11687.45	371.55	6.15	11682.02	366.12	5.43	0.72
23 RH	11323.6	11688.7	365.1	11697.2	373.6	8.5	11692.14	368.54	5.06	3.44
53 RH	11392.8	11753.7	360.9	11778.89	386.09	25.19	11762.61	369.81	16.28	8.91
75 RH	11300	11665.7	365.7	11739.07	439.07	73.37	11713.37	413.37	25.7	47.67
85 RH	11005.1	11369.6	364.5	11474.48	469.38	104.88	11439.28	434.18	35.2	69.68
100 RH	11006.5	11372	365.5	11546.37	539.87	174.37	11479.19	472.69	67.18	107.19

Table 16: Values of the masses for the 1-month BTC experiment.

BTC	**1 month**									
A	**b**	**c**	**d=c-b**	**e**	**f=e-b**	**g**	**h**	**i=h-b**	**j**	**k**
11 RH	10886	11245.6	359.6	11250.52	364.52	4.92	11250.1	364.1	0.42	4.5
23 RH	11309.2	11670.5	361.3	11680.85	371.65	10.35	11679.85	370.65	1	9.35
53 RH	11692.6	12052.8	360.2	12068.75	376.15	15.95	12063	370.4	5.75	10.2
75 RH	11369	11738.4	369.4	11829.59	460.59	91.19	11804.55	435.55	25.04	66.15
85 RH	11033.1	11394.6	361.5	11516.82	483.72	122.22	11481.78	448.68	35.04	87.18
100 RH	11375.1	11741.3	366.2	11962.57	587.47	221.27	11867.47	492.37	95.1	126.17

Table 17: Values of the masses for the 2-month BTC experiment.

BTC	**2 months**									
A	**b**	**c**	**d=c-b**	**e**	**f=e-b**	**g**	**h**	**i=h-b**	**j**	**k**
11 RH	11342.1	11698.1	356	11705.21	363.11	7.11	11705.1	363	0.11	7
23 RH	10960.5	11318.7	358.2	11349.37	388.87	30.67	11347.96	387.46	1.41	29.26
53 RH	10946.7	11300.8	354.1	11364.42	417.72	63.62	11355.68	408.98	8.74	54.88
75 RH	11020.7	11381.7	361	11488.54	467.84	106.84	11463.44	442.74	25.1	81.74
85 RH	11058.7	11420.6	361.9	11560.01	501.31	139.41	11521.58	462.88	38.43	100.98
100 RH	11026.5	11392.1	365.6	11632.74	606.24	240.64	11527.1	500.6	105.64	135

8.3 Sky Springs (SS)

Table 18: Values of the masses for the 1-day SS experiment.

SS	1 day									
A	**b**	**c**	**d=c-b**	**e**	**f=e-b**	**g**	**h**	**i=h-b**	**j**	**k**
11 RH	11253.7	11612.3	358.6	11612.78	359.08	0.48	11612.75	359.05	0.03	0.45
23 RH	11418.4	11797.6	379.2	11798.6	380.2	1	11797.7	379.3	0.9	0.1
53 RH	11280.7	11668.5	387.8	11675.1	394.4	6.6	11673.4	392.7	1.7	4.9
75 RH	11436	11811	375	11826.4	390.4	15.4	11822.3	386.3	4.1	11.3
85 RH	11389.6	11759.3	369.7	11778	388.4	18.7	11772.8	383.2	5.2	13.5
100 RH	11063.1	11430.1	367	11459	395.9	28.9	11450.3	387.2	8.7	20.2

Table 19: Values of the masses for the 2-day SS experiment.

SS	2 days									
A	**b**	**c**	**d=c-b**	**e**	**f=e-b**	**g**	**h**	**i=h-b**	**j**	**k**
11 RH	10640.9	10981.5	340.6	10981.75	340.85	0.25	10979.73	338.83	2.02	-1.77
23 RH	10567.2	10957.8	390.6	10961.3	394.1	3.5	10958.9	391.7	2.4	1.1
53 RH	10690.5	11059.9	369.4	11065.3	374.8	5.4	11062.8	372.3	2.5	2.9
75 RH	10639.8	11039.9	400.1	11061.1	421.3	21.2	11055	415.2	6.1	15.1
85 RH	10573.5	10951.1	377.6	10982.2	408.7	31.1	10973.3	399.8	8.9	22.2
100 RH	10556.1	10911.8	355.7	10958.6	402.5	46.8	10945.1	389	13.5	33.3

Table 20: Values of the masses for the 1-week SS experiment.

SS	1 week									
A	**b**	**c**	**d=c-b**	**e**	**f=e-b**	**g**	**h**	**i=h-b**	**j**	**k**
11 RH	10543.2	10904.4	361.2	10908.76	365.56	4.36	10904.8	361.6	3.96	0.4

23 RH	10701.9	11066.5	364.6	11073.25	371.35	6.75	11067.57	365.67	5.68	1.07
53 RH	10674.8	11036.6	361.8	11043.97	369.17	7.37	11041.3	366.5	2.67	4.7
75 RH	10485.3	10849.99	364.69	10876.2	390.9	26.21	10866.63	381.33	9.57	16.64
85 RH	10538.9	10902.7	363.8	10947.47	408.57	44.77	10934.34	395.44	13.13	31.64
100 RH	10533.5	10897.7	364.2	10991.01	457.51	93.31	10961.82	428.32	29.19	64.12

Table 21: Values of the masses for the 2-week SS experiment.

SS	**2 weeks**									
A	**b**	**c**	**d=c-b**	**e**	**f=e-b**	**g**	**h**	**i=h-b**	**j**	**k**
11 RH	10552.3	10917.2	364.9	10921.08	368.78	3.88	10918.92	366.62	2.16	1.72
23 RH	10607	10969.6	362.6	10976.76	369.76	7.16	10973.11	366.11	3.65	3.51
53 RH	10447.1	10813.7	366.6	10835.55	388.45	21.85	10830.36	383.26	5.19	16.66
75 RH	10597.2	10960.3	363.1	11004.66	407.46	44.36	10991.72	394.52	12.94	31.42
85 RH	10642.7	11003.8	361.1	11072.91	430.21	69.11	11051.43	408.73	21.48	47.63
100 RH	10546.4	10908.1	361.7	11050.87	504.47	142.77	11000.81	454.41	50.06	92.71

Table 22: Values of the masses for the 1-month SS experiment.

SS	**1 month**									
A	**b**	**c**	**d=c-b**	**e**	**f=e-b**	**g**	**h**	**i=h-b**	**j**	**k**
11 RH	10562.7	10921.9	359.2	10926.45	363.75	4.55	10928.84	366.14	-2.39	6.94
23 RH	10491.5	10854.3	362.8	10862.72	371.22	8.42	10864.75	373.25	-2.03	10.45
53 RH	10573.1	10934.8	361.7	10948.89	375.79	14.09	10946.45	373.35	2.44	11.65
75 RH	10580	10938.2	358.2	11008.94	428.94	70.74	10995.43	415.43	13.51	57.23
85 RH	10620.1	10979.1	359	11081.75	461.65	102.65	11058.32	438.22	23.43	79.22
100 RH	10554.4	10913.7	359.3	11104.09	549.69	190.39	11021.87	467.47	82.22	108.17

Table 23: Values of the masses for the 2-month SS experiment.

SS	**2 months**									
A	**b**	**c**	**d=c-b**	**e**	**f=e-b**	**g**	**h**	**i=h-b**	**j**	**k**
11 RH	10636.3	10997.9	361.6	11009.83	373.53	11.93	11005.59	369.29	4.24	7.69
23 RH	10587.2	10949.4	362.2	10973.29	386.09	23.89	10965.45	378.25	7.84	16.05
53 RH	10550.6	10915.5	364.9	10956.26	405.66	40.76	10945.82	395.22	10.44	30.32
75 RH	10578.5	10940.5	362	11042.51	464.01	102.01	11024.68	446.18	17.83	84.18
85 RH	11055	11420.4	365.4	11623.77	568.77	203.37	11526.62	471.62	97.15	106.22
100 RH	10918.9	11283.7	364.8	11524.89	605.99	241.19	11413.62	494.72	111.27	129.92

9. Vita

Pedro Josué Hernández Penagos earned his bachelor's degree in physics from the Autonomous University of Chiapas *(Spanish: Universidad Autónoma de Chiapas*), Mexico, in January 2020. He commenced his graduate courses in August 2022 by enrolling in the Master of Science in Physics program at the University of Texas at El Paso (UTEP). In September of the same year, he became a member of the Nanomaterials, Interfaces, and Confinement for Energy and the Environment ($NICE^2$) research group, under the leadership of Dr. José Leobardo Bañuelos. During the Fall 2022 semester, Pedro served as a Graduate Teaching Assistant. With the onset of the Spring 2023 semester, he transitioned to a Graduate Research Assistant role, contributing to a Department of Energy-funded project in collaboration with Oak Ridge National Laboratory (ORNL). In the Summer of 2023, as a Graduate Research Summer Intern at ORNL, Pedro conducted experiments, the results of which, along with those obtained at UTEP, were showcased at the American Physics Society (APS) March Meeting 2024 in Minneapolis, Minnesota. In April 2024, Pedro's academic path led him to acceptance into the PhD program in Physics at UTEP, where he will continue his research endeavors starting Fall 2024, under the esteemed guidance of Dr. Bañuelos.